Impact of the formation angle on the drag of bio-inspired ∨ formations

Prasoon Suchandra
Woodruff School of Mechanical Engineering, Georgia Institute of Technology, Atlanta, Georgia 30332, USA

Shabnam Raayai-Ardakani*
Department of Mechanical Engineering, Boston University, Boston, Massachusetts 02215, USA

(Received 24 April 2026; accepted 6 August 2026; published 31 August 2026)

Bio-inspired ∨ flight formation is a well-known technique for energy saving among groups of fixed-wing aircraft, and as of recently, for groups of quad-rotors. Here we study the effect of the formation angle on the performance of each of the members of a five-member ∨ formation in terms of the flow field, and drag force. We employ axisymmetric cylinders, which are nonlifting in solo condition to reduce or eliminate the effect of the lift (lateral force) on the group performance, and use time-resolved, multi-illumination, consecutive-overlapping particle image velocimetry (PIV) to capture the velocity field around and between the members. Over a range of ∨-formation angles, we see various degree of drag reduction, with the highest drag reduction (∼80%) for the interior members of the tightest formation (formation with the smallest ∨ angle and the most overlap in frontal views). All formation members experience some levels of drag reduction up to a ∨ angle of around 50°, and in a formation with a ∨ angle greater than 50°, only the leading member experiences observable drag reduction. We explore the complex flow dynamics between the formation members in terms of wake-body and wake-wake interactions and the bleeding (gap) flow. We present the mean and fluctuating quantities, as well as the dynamics of the vortex shedding and circulation in the wakes of the members, and discuss how these flow characteristics relate to the drag of each member, as a function of both their position within the ∨ and the angle of the formation. This current study serves as a baseline for further explorations of wake-body and wake-wake interactions of flow past groups of bodies and demonstrates how changing formation angle can help achieve a desired group performance (like minimum drag).

DOI: 10.1103/m9ny-j9bd

I. INTRODUCTION

A ∨ formation is a common travel pattern seen among groups of migratory birds, including but not restricted to Canada geese [1–3], pelicans [4], pigeon flocks [5], and Northern bald ibises [6] with recorded energetic and psychological benefits for the birds [4]. Formation flight of fixed wing aircraft, especially ∨ formations, have also shown energetic benefits compared with a single aircraft, with more military implementation of this flight strategy than commercial ones. More generally, group motion is a common behavior among animals, examples ranging from insect swarms [7–9] and schools of fish [10–16] to other aquatic life forms [17]. Geometric arrangements in flow conditions are also observed in mangrove vegetation patches in riverfront and coastal areas which are able to control flood and prevent soil erosion [18–23]. Studies of flow past solid arrays are also essential for engineering applications, such as heat

*Contact author: shraayai@bu.edu

exchangers in power plants [24–26], and designs of marine structures [23,24,27]. Different speed sports such as speed skating and cycling use different drafting techniques in competitions as well [28,29].

Formation flights of birds and fixed wing aircraft have been mainly explored based on the potential flow analysis of the wing-tip vortices of a finite-span lift-generating body and the lift-induced upwash outside the wake [30–39]. However, in recent years, application of formation strategies for drone swarms has shown promise in managing and controlling the battery consumption of groups of rotorcraft [40]. With the differences in the flight mechanism of the fixed and rotary-wing systems, the potential flow model of formation based on lift-induced upwash does not readily apply to the new generation of vehicles, including those in air and in water. Previously, as proof of concept, we have shown that using non-lift-generating cylinders in a $\vee$ formation allows us to alter the drag force experienced by the members of a formation. Using two nominal formation angles of 36.87° (Narrow) and 67.38° (Wide), we reported that the Narrow formation, where members have frontal overlaps, is able to reduce the drag force experienced by all the bodies, while with the Wide formation, only the drag of the leading member of the formation was reduced [41]. Therefore, with the concept established, understanding the mechanics of flow around arrangements of objects, specifically with a focus on the impact of the variations in the geometry of the formation on the dynamic response of the flow, can be effectively used as an optimization tool and design guide for tuning the aero- and hydrodynamic responses, like minimizing energy expenditure for a group of vehicles.

Here we study the effect of the $\vee$ angle on the aero- and hydrodynamic performance of $\vee$ formation of five nonlifting members, i.e., cylinders. Expanding on our simplified binary approach, we perform a parameter sweep across 10 formation angles to explore how the nonlinear wake-wake and wake-body interactions impact the kinematic and dynamic response of the flow field, with a specific focus on drag force. We employ cylinders as canonical models of nonlifting objects [42] and focus on five-member groups as an intermediate representatives that capture many of the qualities of three- and seven-member dynamics as previously discussed [41]. While some of the flow patterns in formations with five and seven members [41] show similarities with the patterns previously studied for side-by-side cylinders [43–45], as well as cylinders in tandem and staggered arrangements of two or three cylinders [45–50], those qualitative interference patterns are not sufficient to describe the flow interactions in formations with a larger number of members [48], including $\vee$ formations. We present a high resolution and quantitative experimental exploration and employ a multi-light-sheet [41,51] approach to overcome the challenge of shadows in the presence of multiple bodies which has limited the previous studies to views of flows on only one side, or the wakes [18,52]. We also recognize the challenges associated with implementation and use of index-matched facilities, including limited material availability, high costs, and the potential hazards of specialized fluids which make such facilities impractical [53,54] and use the multi-light-sheet approach as a cost-effective alternative to index matching. In addition, we use a consecutive-overlapping imaging approach which allows us to capture a larger area of interest around the formations at high resolution [41,51,55,56]. We use the experimental results and the progressive sweep of the formation angle to explore the dynamics of wake-wake and wake-body interactions beyond what the two categories of Narrow and Wide formations offer [41], focusing on the interactions of the shear layers of each body with one another and with the wakes, and how they regulate the flow field.

This paper is organized as follows: in Sec. II we give an overview of the experimental setup and procedures, and discuss the results in Sec. III. In Sec. III A we present the drag coefficients of each member as a function of their location within the array and the $\vee$-formation angle ϕ, and discuss the general trends. In Secs. III B and III C we continue to explore the velocity and pressure distribution around the members and how the variations in the flow fields affect the forces experienced by each member as the formation angle is changed and how does this affect the overall performance of the group. In Sec. III D we present a preliminary overview of some of our observations in the potential changes in lift experienced by the bodies, and the temporal variation of the circulation in the wakes

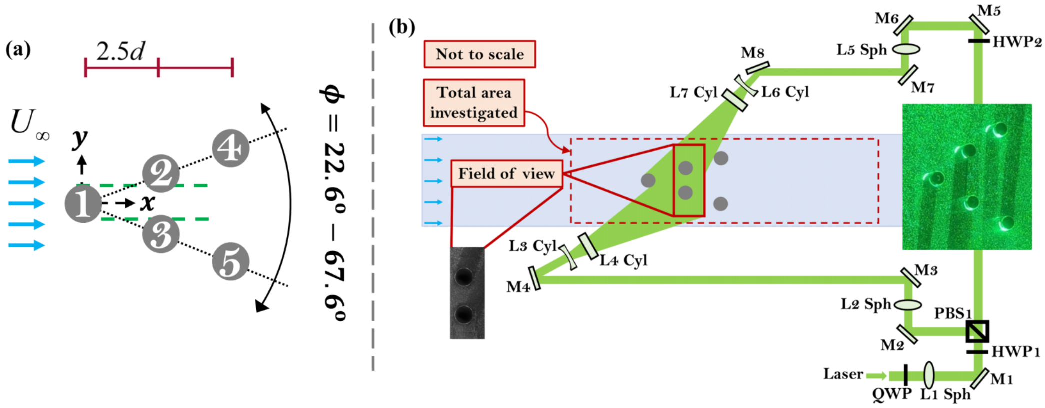

FIG. 1. (a) Schematic summary of the ∨ formations, along with the member numbering and the coordinate system. (b) Schematic of an angled double-sheet laser illumination for visualizing the flow inside and around a multibody sample. The view of the intersection of the two light sheets around the array members is also shown from the bottom of the test section.

and the vortex shedding pattern. Eventually in Sec. IV we highlight the main takeaways from the current study.

II. METHODS

A. Geometric setup

To study the dynamics of flow around formations of nonlifting objects, the ∨ formations here are designed as a symmetric, two-echelon linear configuration, where the formation angle of the ∨, called ϕ, is the angle between the two echelons or branches [41]. Here, we consider a group of five stationary nonlifting circular cylinders of diameter $d = 6\,\text{mm}$, arranged in ∨ formations [Fig. 1(a)]. We keep the horizontal distance between the rows of the members constant at $2.5d$ which is slightly lower than the vortex formation length [41,42,57–61] of a single cylinder ($\sim 2.6d$) at the given conditions and within the region of "wake interference" [48]. Due to the physical limit, the lowest possible ϕ is 22.6°, where members 2 and 3 are in contact which corresponds to the "touching line" as previously noted in studies of two and three cylinders or pipes in tandem [48]. Independent of the results, we divide the experimental cases here into two categories, with the first one comprising the formations where the members have streamwise overlaps along each echelon, or $\phi < \phi^* = 43.6^\circ$, and the second group consisting of formations with no frontal overlaps among the members, corresponding to $\phi > \phi^* = 43.6^\circ$. This streamwise or frontal extent is indicated by green dashed lines for members 1, 2, and 3 in Fig. 1(a). We extend the investigation, in 5° steps up to $\phi = 67.6^\circ$ where the flow past all the members almost (but not quite) resembles that of five isolated members [41] and the drag measurement plateaus for two consecutive angles. Overall, we present 10 cases and explore how varying ϕ can help to achieve a specific desired group performance (like minimum drag).

B. Experimental procedure

Our experiments are conducted in a water tunnel facility [41,51,55,56], with a test section of 20 cm × 27 cm in cross section and 2 m in length. The water height is kept at about 20 cm during the experiments. All experiments are performed at free-stream speed of $U_\infty \approx 17.7$ cm/s with run-to-run variation of ±0.3 cm/s. The Reynolds number based on this free-stream speed and cylinder diameter d is $\text{Re}_d \approx 1100$, corresponding to a turbulent wake behind a single circular cylinder [62,63]. $\mathrm{Re}_d = 1100$ falls within the regime where cylinders maintain a nearly constant $C_D \approx 1$ over a broad range of Reynolds numbers [64]. Furthermore, based on Strouhal-Reynolds curves [62], around this Reynolds number, we can record near-maximum Strouhal number in this flow regime.

The velocity field around the sample is obtained via a time-resolved two-dimensional, two-component (2D-2C) particle image velocimetry (PIV) system [65–67], as shown in Fig. 1(b). It consists of a double-pulsed Nd:YLF laser (Terra PIV, Continuum Laser) of 527 nm (green light), a high-speed camera (Chronos 2.1, Kron Technologies Inc.) at a resolution of 720×1920 pixels with a 100 mm macro lens (Canon EF 100 mm f/2.8L Macro Lens), and a timing unit (Arduino Teensy Board [51,68]) synchronizing the laser pulses and camera capture. The imaging magnification is set to each pixel capturing about 18 μm. The delay between the two successive laser pulses for the PIV is set at $\delta t = 1000$ μs. The laser is operated at a frequency of 500 Hz (note that the vortex shedding frequency of a single cylinder at $\mathrm{Re}_d \approx 1100$ is around 6 Hz). Water is seeded with 8–12 μm hollow glass particles (TSI Inc.) as PIV tracers.

To illuminate the field of view around the array members, we use an angled double-light sheet strategy as shown in Fig. 1(b), which is an updated variation of the multi-light-sheet strategies of Fu and Raayai-Ardakani [55] and Fu, Suchandra, and Raayai-Ardakani [51] implemented for high-frequency, time-resolved acquisition. The optical components are arranged such that the incoming laser beam is divided into two beams using a half-wave plate (HWP) and a polarizing beam splitter (PBS) and directed toward the front and back of the tunnel through multiple mirrors (M). Additionally, a HWP and a quarter-wave plate (QWP) are used to get the proper polarity of the beams on the two sides, getting the best possible illumination in the camera's field of view. The beams are passed through a combination of spherical (Sph) and cylindrical (Cyl) lenses, illuminating the field of view as demonstrated in Fig. 1(b). (Note that the combination of laser optics used depends on the type of laser, camera and the intended application.) Each laser sheet is about 2 mm in thickness. Formations with small ϕ (i.e., those with streamwise overlaps between members; $\phi < 43.6^\circ$) result in dark spots between various members (in particular, between members 2 and 3). In such cases, with a slight change in the angle of the light sheet, we can illuminate the dark area while placing a different region in shadow [41]. In these cases, the field of view is imaged more than once so that each portion of the field of view is illuminated (without shadow) in at least one set of images [41].

The camera is traversed throughout the total area of interest via a computer numerically controlled (CNC) carrier in consecutive-overlapping steps [51,55]. The imaging is repeated across the streamwise length (x direction) with about 30% overlap and the normal width (y direction) with about 20%–50% overlap (case-to-case variations) with the previous position [41]. The laser sheet optics are moved manually. PIV is performed for image pairs captured at each location and the results are stitched to get the full velocity field. At each field of view, 990 PIV image pairs are captured, which are found to be sufficient for the convergence of the mean and fluctuation quantities [41].

The PIV image pairs are processed using the open-source software OpenPIV [69]. The PIV search area is 64 px × 64 px in size and the interrogation window is 32 px × 32 px with 87.5% overlap (28 px) with the neighboring windows. The resolution of the processed data is ∼80 μm per vector. Spurious PIV data are detected and removed using the universal outlier detection method of Westerweel and Scarano [70].

C. Force calculations

With the PIV data, we calculate the drag forces experienced by each member using a control volume analysis, as discussed in detail by Suchandra and Raayai-Ardakani [41]. In summary, we apply the conservation of mass and momentum fluxes through an appropriately chosen control volume (CV) around an entire formation as well as each of its members and use the

Reynolds-averaged integral momentum (RAIM) conservation equation [22,41,55] as given by

$$D\boldsymbol{e}_x + L\boldsymbol{e}_y = \underbrace{-\rho\int_{\mathrm{CS}}\overline{(\boldsymbol{u}+\boldsymbol{u}')[(\boldsymbol{u}+\boldsymbol{u}')\cdot\boldsymbol{n}]}dA \;+\; D_{3\mathrm{D}}\boldsymbol{e}_x + L_{3\mathrm{D}}\boldsymbol{e}_y}_{\text{Momentum fluxes, Reynolds stresses, and 3D effects}} \;\underbrace{+\int_{\mathrm{CS}}\boldsymbol{n}\cdot\overline{\boldsymbol{\tau}}dA}_{\text{Viscous forces}}\underbrace{-\int_{\mathrm{CS}}p\,\boldsymbol{n}\,dA}_{\text{Pressure forces}}, \tag{1}$$

which provides the drag and lift forces (on the body enclosed in the CV) per unit length of the cylinder, D and L, respectively and $\boldsymbol{e}_x$ and $\boldsymbol{e}_y$ are the unit vectors in each of the corresponding directions, and CS denotes the control surface. Here ρ and μ are the density and dynamic viscosity of the fluid (water) respectively, $\overline{(\ldots)}$ denotes ensemble-averaging, $\boldsymbol{\tau}$ is the stress tensor, p is the pressure, and $\boldsymbol{n}$ is the local outward unit normal vector to the control surface. $D_{3\mathrm{D}}$ and $L_{3\mathrm{D}}$ are correction terms for the out-of-plane momentum fluxes not captured using planar PIV, and are calculated following the method described by Fu and Raayai-Ardakani [55]. We employ the Reynolds decomposition [64] and decompose the instantaneous velocity vector $\tilde{\mathbf{u}}(x,y,t)$ into the mean $\mathbf{u}(x,y)$ and the fluctuating component $\mathbf{u}'(x,y,t)$, as $\tilde{\mathbf{u}}(x,y,t)=\mathbf{u}(x,y)+\mathbf{u}'(x,y,t)$. In the current work, contribution of the shear stresses to the viscous forces on the outer boundaries of the CV are not neglected as these boundaries are sufficiently close to the enclosed solid as previously discussed [41], especially when calculating the drag force on an individual member of the formation. As for the pressure distribution, we use the velocity field from the PIV and line integration [71–77] of the pressure gradient terms in the Reynolds-averaged Navier-Stokes (RANS) equations [64,78,79] to obtain the mean pressure as given by

$$p(x)-p(x_{\mathrm{ref}})=\int_{x_{\mathrm{ref}}}^{x}\left[-\rho\left(u\frac{\partial u}{\partial x}+v\frac{\partial u}{\partial y}\right)+\mu\left(\frac{\partial^2 u}{\partial x^2}+\frac{\partial^2 u}{\partial y^2}\right)-\rho\left(\frac{\partial\overline{u'u'}}{\partial x}+\frac{\partial\overline{u'v'}}{\partial y}\right)\right]dx, \tag{2}$$

$$p(y)-p(y_{\mathrm{ref}})=\int_{y_{\mathrm{ref}}}^{y}\left[-\rho\left(u\frac{\partial v}{\partial x}+v\frac{\partial v}{\partial y}\right)+\mu\left(\frac{\partial^2 v}{\partial x^2}+\frac{\partial^2 v}{\partial y^2}\right)-\rho\left(\frac{\partial\overline{u'v'}}{\partial x}+\frac{\partial\overline{v'v'}}{\partial y}\right)\right]dy, \tag{3}$$

where u and v are the streamwise and normal components of the mean velocity vector respectively. Using the above analysis, we employ at least 20 different control volumes around each cylinder, and report the mean values and their 95% confidence intervals in the upcoming figures.

D. Bleeding flow

The flow passing through the spacing between formation members, called the "bleeding flow" or the "gap flow" [21,27,44,45,80–82], has a significant effect on the forces experienced by the members [41]. Here, we mark the mean velocity of the flow through the gap between the members as $\boldsymbol{u}_{ij}^b$ with i and j referring to the relevant member numbers. We also define the equivalent bleeding flow, U_{ij}^b, between any two array members i and j which is calculated by dividing the total volumetric flow rate (per unit length of the cylinder) between the two members by the linear distance between those two members, as given by

$$U_{ij}^b=\frac{\left|\int_A \boldsymbol{u}_{ij}^b\cdot\boldsymbol{n}\,dA\right|}{\int_A dA}=\frac{\left|\int_i^j \boldsymbol{u}_{ij}^b\cdot\boldsymbol{n}\,L_z\,d\ell_{ij}\right|}{\int_i^j L_z\,d\ell_{ij}}=\frac{\left|\int_i^j \boldsymbol{u}_{ij}^b\cdot\boldsymbol{n}\,d\ell_{ij}\right|}{\ell_{ij}}, \tag{4}$$

where $dA=L_z\,d\ell_{ij}$ is the infinitesimal area element (L_z is the length of a member in the z direction, perpendicular to x-y plane), $\boldsymbol{n}$ is the normal to the area element, $|\ldots|$ denotes the magnitude, and ℓ_{ij} is the shortest linear distance between the surfaces of the two members. Note that i and j symbolically denote member numbers and do not refer to the actual geometric positions of the integral bounds on the surfaces of the members in the x-y plane (see Supplemental Material [83] Sec. SM.A for more details on the bleeding flow calculations).

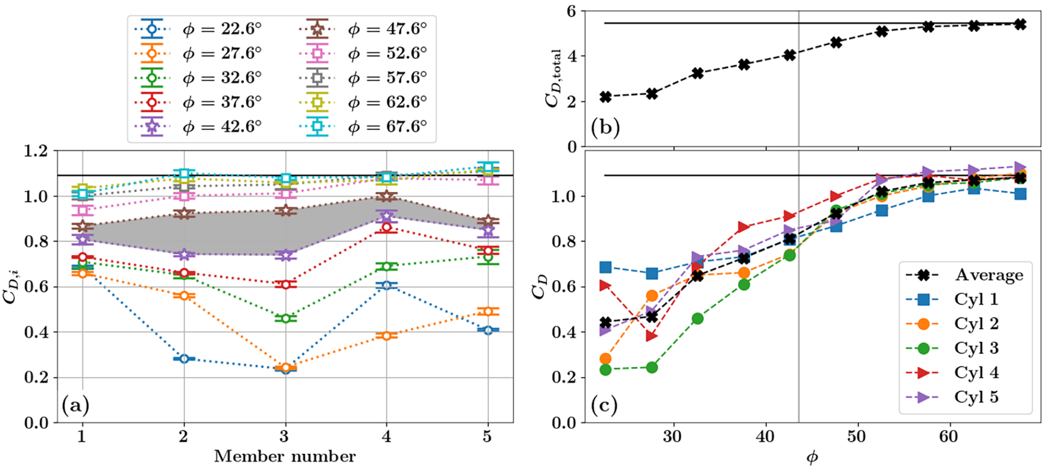

FIG. 2. (a) Ensemble-averaged drag coefficient, $C_{D,i}$, for all the individual members of all the ∨ formations as a function of the member number. Error bars are based on 95% confidence intervals. Overlapping formations are designated with round symbols, nonoverlapping formations are shown with square symbols, and the two formations close to the crossover $\phi^* = 43.6°$ are marked with star symbols and the separation is colored in light gray for visibility. (b) Total ensemble-averaged drag coefficient, $C_{D,\text{total}}$, against angle of ∨, ϕ, for all the formations. The crossover angle $\phi^* = 43.6°$ is marked with a gray vertical line. (c) Drag coefficient, $C_{D,i}$, of (a) replotted as a function of the formation angle ϕ. Members of the same row are shown with the same symbols and different colors. The black dashed line corresponds to the average drag of the group, $C_{D,\text{total}}/5$.

III. RESULTS

A. Drag force experienced by each member

We start by examining the drag forces on each individual member of the different ∨ formations, as defined by $C_{D,i} = D_i/(0.5\rho U_\infty^2 d)$ for member i, and the drag of the entire formation as one group, denoted by $C_{D,\text{total}}$, presented in Fig. 2. We present the drag force of individual members as a function of their member numbers (i.e., positions) in Fig. 2(a) for the various formations, the total drag of the entire formation as a function of the formation angle in Fig. 2(b), and replot the drag of individual members, this time as a function of the formation angle in Fig. 2(c) for clarity. To facilitate comparison across the cases, the denominators of the drag coefficients are kept constant according to the *a priori* knowledge of the geometry and the flow $(0.5\rho U_\infty^2 d)$. The measured drags at $\phi = 37.6°$ and $67.6°$ are close to the values reported previously for $\phi = 36.87°$ and $\phi = 67.38°$ [41], confirming the reproducibility of the results.

The trends in the drag force vary both as a function of the angle of the formation, and the position of the members [indicated with numbers shown on the cylinders in the Fig. 1(a) and upcoming figures]. At a first glance, as seen in Fig. 2(a), the two categories of overlapping and nonoverlapping formations defined in Sec. II A, separate the drag responses into two groups where on the figure, the space between the two cases that are at the margin of the overlap, i.e., $\phi = 42.6°$ and $\phi = 47.6°$ is colored in gray. But after a careful observation, the patterns of the drag force of individual members of $\phi = 47.6°$ formation show a closer resemblance to the overlapping cases than the nonoverlapping cases.

For formations with $\phi \leqslant 47.6°$, all members experience significant reductions in the drag force, with asymmetries in the C_D of members of the same row (comparing 2 against 3, and 4 against 5). At lower angles with larger frontal overlaps, especially $22.6° \leqslant \phi \leqslant 37.6°$, the flow becomes asymmetric (asymmetry about the $y = 0$ line) resulting in different drag forces on members of the upper and lower echelons and will be discussed further in Secs. III B and III C. For formations with $\phi \geqslant 52.6^\circ$, we see minimal reductions in the drag force compared with the case of the single cylinder, where the main benefit goes to the leading member 1. In these cases, the trend in the drag coefficient is more uniform: member 1 has the lowest drag, followed by slightly higher drag measured for members 2 and 3, and then the highest values going to members 4 and 5 [see Fig. 2(a)].

The total drag force on the entire formation [Fig. 2(b)] increases monotonically with the formation angle. For $\phi \lessapprox 60^\circ$, the total drag is less than the total drag if each member behaved like an isolated cylinder, i.e., $C_{D,\text{total}} < 5 \times C_D^{\text{iso cyl}}$. Thus, even without streamwise overlaps, ∨ formations can offer a lower total drag and such nonoverlapping formations are viable options for managing the energy consumption within groups. The increase in the angle of the formation, results in a consistent increase in the drag force on each member, except for member 4 in $\phi = 22.6^\circ$ and 27.6° formations, mainly due to the asymmetries seen in $\phi = 22.6^\circ$ and $\phi = 27.6^\circ$ cases. For the leading member 1, drag force takes a mild increasing trend, starting from $C_{D,1} \approx 0.67$ for $\phi \leqslant 27.6^\circ$, then increasing monotonically for $32.6^\circ \leqslant \phi \leqslant 52.6^\circ$, and asymptotically reaching $C_{D,1} \approx 1$ for $\phi \geqslant 57.6^\circ$. In addition, the leading member takes advantage of the presence of members 2 and 3 in the second row, which directly lie in the path of the wake of member 1. This results in a pressure recovery downstream (or equivalently, the leading member receiving a "forward push" from downstream members 2 and 3) [41], leading to a reduced drag compared to a solo cylinder case (see more in Secs. III B and III C).

In Fig. 2(c) member 1 experiences the highest drag of the group at lower angles, and crosses over to less than the trailing members and more than the C_D of the middle row at intermediate angles (all overlapping), and has the lowest drag of the formation for all nonoverlapping angles. As the formation angle increases, especially past ϕ^*, we see the drag force of interior and trailing members asymptotically approach the drag of a solo case. This is especially visible for members 2 and 3 in $\phi > 60^\circ$, and members 4 and 5 in $\phi > 50^\circ$, with member 5 slightly exceeding the drag force of the solo case at the two largest formation angles. Member 1, on the other hand, maintains a lower drag force than the solo case. The lowest drag force among all members and cases tested occurred for member 3 of the $\phi = 22.6^\circ$ and 27.6° formations ($C_D \approx 0.24$), followed by member 2 of the $\phi = 22.6^\circ$ ($C_D \approx 0.28$).

B. Flow pattern through ∨ formations

To explore the mechanism of variations in the drag force of each member ($C_{D,i}$) compared to a solo cylinder, presented in Sec. III A, we examine the velocity field past the formations from both global (this section) and local (see Sec. III C) points of view. Figures 3 and 4 present the contours of the normalized mean streamwise, $u(x, y)/U_\infty$, and normal velocities, $v(x, y)/U_\infty$, in and around the formations. The velocity contours of the solo cylinder case are presented above the subfigures for comparison. Figures 3(a)–3(e) and 4(a)–4(e) correspond to formations with frontal overlaps among the members, and Figs. 3(f)–3(j) and 4(f)–4(j) represent the formations without frontal overlaps. The magnitudes and inward/outward direction of the bleeding flows between members of each echelon of the formations are shown in the subfigures of Fig. 3 as well. Bleeding flow between members of the same row are shown in Tbl. SM.1 in the Supplemental Material [83]. To accompany the contour plots, emphasize the importance of bleeding flows, and identify the flow features that contribute to the composition of the bleeding flow, we also present the distribution of the streamlines of the mean flow calculated via integration starting from a point along the global $x = -d$ line upstream of the leading member as shown in Fig. 5.

To visualize the flow patterns, the streamlines in Fig. 5 are color coded by trajectory, with each separate color distinguishing groups of streamlines passing between or on the side of specific members and identify between the bleeding or external flows. The streamline groups are separated based on the position of the stagnation points on the members where they divide into separate streams on either side of the body. The upper- and lower-most groups are the streamlines passing on the exterior of members 4 and 5, and denoted by Ext 4 and Ext 5. The two middle groups, are the streamlines that pass in the interior in between members 2 and 4 on the upper echelon, called Int

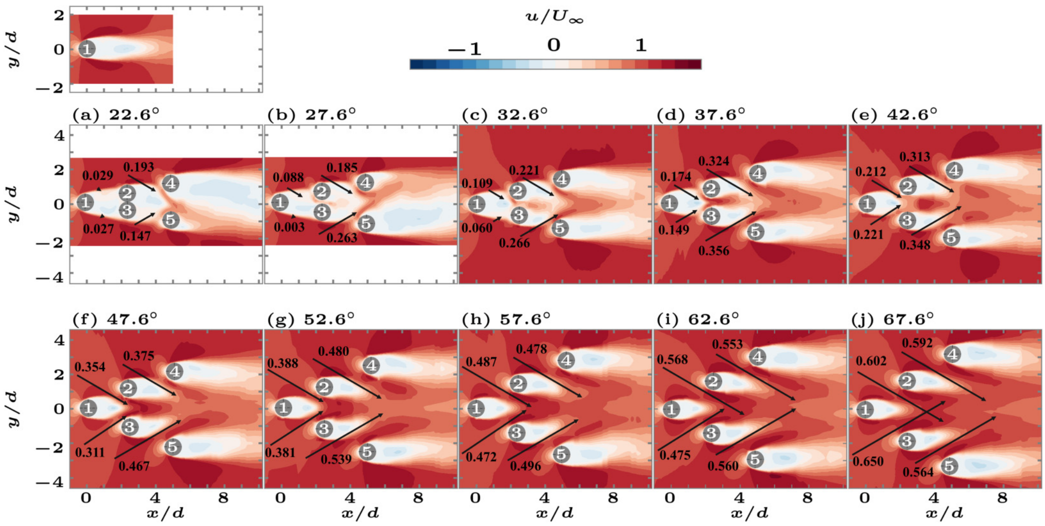

FIG. 3. Contours of normalized mean streamwise velocity, $u(x, y)/U_\infty$ for formations with ϕ going from 22.6° to 67.6° in steps of 5°. Panels (a)–(e) correspond to the cases with frontal overlaps, and panels (f)–(j) correspond to the cases with no frontal overlaps. The velocity contours for the solo cylinder is presented on the top as reference. The magnitude of the bleeding flow, U^b_{ij}/U_∞, between the members of each echelon of the formation are shown on the figures. Arrows are shown to indicate inward and outward flow and are not accurate representation of the average direction of the flow. Arrows' lengths are proportional to the magnitude of the bleeding flow.

2,4 (constituting the $\boldsymbol{u}^b_{24}$ bleeding flow), and members 3 and 5 on the lower echelon, called Int 3,5 (constituting the $\boldsymbol{u}^b_{35}$ bleeding flow). Similarly, the two streamline groups in the interior and between members 1 and 2 on the upper echelon, are called Int 1,2 ($\boldsymbol{u}^b_{12}$ bleeding flow) and 1 and 3 on the

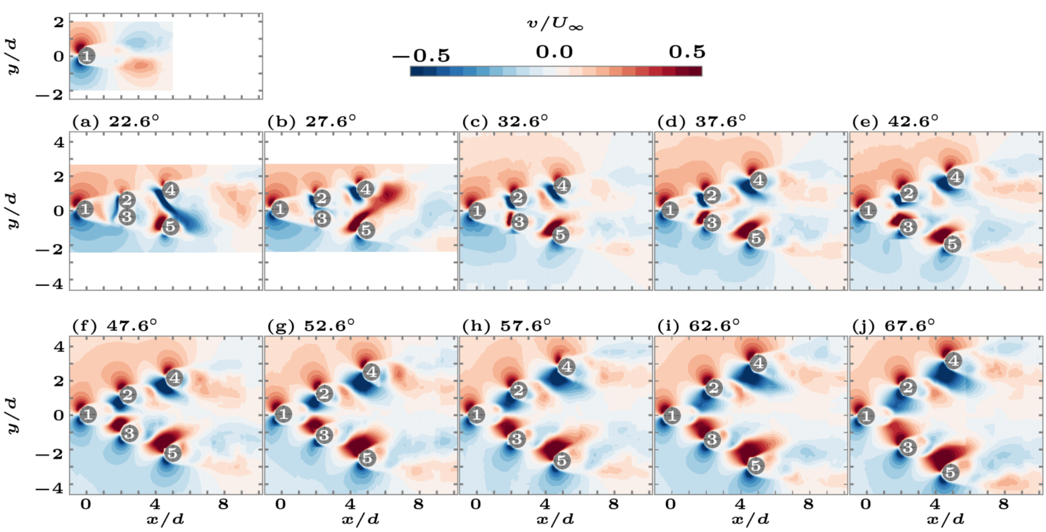

FIG. 4. Contours of normalized mean normal velocity, $v(x, y)/U_\infty$ for formations with ϕ going from 22.6° to 67.6° in steps of 5°. Panels (a)–(e) correspond to the cases with frontal overlaps, and panels (f)–(j) correspond to the cases with no frontal overlaps. The velocity contours for the solo cylinder is presented on the top as reference.

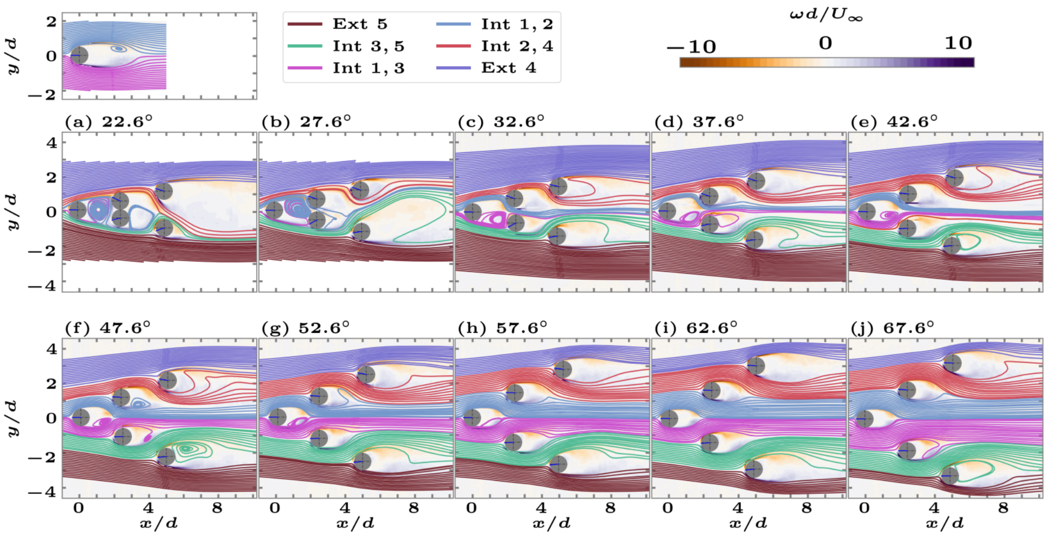

FIG. 5. Streamlines of the flow for formations with ϕ going from 22.6° to 67.6° in steps of 5°. The streamlines are calculated via integration of the velocity fields starting from points along a vertical line at $x/d = -1$ and are color coded based on their trajectory around and between the different members. The dark blue lines inside the cylinders, connecting the centers of the cylinders and their circumferences, denote the location of the frontal stagnation points. The streamlines are overlaid on the mean vorticity contours, also shown in Fig. SM.2 in the Supplemental Material [83] for clarity. The streamlines for the solo cylinder is presented on the top as reference. In the legend, Int i,j refers to streamline groups coinciding with bleeding flows $\boldsymbol{u}^b_{ij}$, and Ext i corresponds to streamlines that pass on the external side of member i.

lower echelon, are called Int 1,3 ($\boldsymbol{u}^b_{13}$ bleeding flow). For the reference solo cylinder, the streamlines on either side of the cylinder are marked with the colors associated with Int 1,2 and Int 1,3 due to the similarity with member 1 of all the formations.

Overall, we observe complex wake-body interactions that evolve as the angle of the ∨ is increased. As ϕ increases, flow around the individual members increasingly resembles one another, especially for trailing members 4 and 5. However, the velocity fields around each of the members consistently show differences compared with the solo cylinder case. Even at the maximum separation here (largest ∨ angle of $\phi = 67.6°$), the wakes and the cylinders remain under influence of the neighbors and do not reach a separation sufficient for the flow to behave as flow past five isolated cylinders. Since drag force is the integral of wall shear stress and pressure, it does not have a one-to-one mapping to flow kinematics, and multiple scenarios of wall shear stress and pressure can result in the same drag value on a cylinder. Therefore, for nonoverlapping formations, cylinders can experience the same drag force as a solo cylinder while being exposed to different velocity fields. In other words, the flow field and drag are not mutually exclusive.

These flow differences, similar to the variations in the drag force (Sec. III A), depend on the formation angle and the position of the member within the formation. On the one hand, the proximity of the bodies, and the choice of the streamwise distance (slightly lower than the vortex formation length), exposes the downstream bodies to the impact of the wakes of the upstream members. On the other, nonlinearities of the governing physics of the flow result in more complex interactions between the flow field past multiple members compared with the solo cylinder case. Overall, by focusing on the progression of formation angles, we capture a more clear picture of the variations in the impact of wake and flow nonlinearities.

Based on velocity contours and streamlines, i.e., flow dynamics, we can categorize the studied cases into three groups following a few distinct patterns beyond that captured by separation into

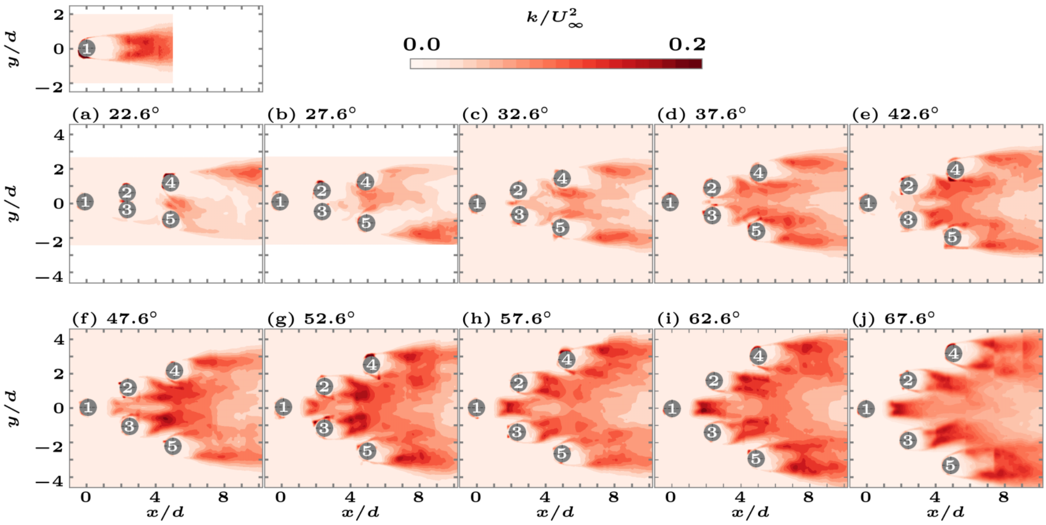

FIG. 6. Contours of normalized turbulent kinetic energy, k/U_∞^2, with ϕ going from 22.6° to 67.6° in steps of 5°. The turbulent kinetic energy contours for the solo cylinder is presented on the top as reference.

Narrow/overlapping or Wide/nonoverlapping formations (used previously): the first group consists of the two lowest angles with overlaps, $\phi = 22.6°$, and 27.6°, where the wake of member 1 encompasses members 2 and 3 and the wakes of the interior members are largely asymmetric about the $y = 0$ line; the second group covers the cases of $\phi = 32.6°$, 37.6°, 42.6°, and 47.6° where the separation bubble in the wake of member 1 consists of two vortices fully enclosed by the streamlines of the bleeding flows $\boldsymbol{u}_{12}^b$ and $\boldsymbol{u}_{13}^b$ and the wakes of the rest of the members, especially members 4 and 5 are affected by the presence of the rest of the members; and the last group covers $\phi \geqslant 52.6°$, where the shape of the wake of the same member stays nearly similar as the angle is changed. We use these qualitative groups to analyze the mechanism of the flow physics in the upcoming subsections.

At the Reynolds number of the experiments here, the wake of a single cylinder becomes turbulent, recording nonzero levels of turbulent kinetic energy (TKE), $k = 0.5(\overline{u'u'} + \overline{v'v'})$, in the wake with the maximum taking place around the formation length of $2.6d$. Therefore, in addition to velocity contours and streamlines, we present the normalized TKE, k/U_∞^2, for the $\vee$ formations in Fig. 6. In the overlapping formations, and especially lower angles, the slower flow in the interior of the array prohibits the flow from transitioning to turbulence (compared with the wake behind an isolated cylinder) and therefore we see lower levels of k in the upstream and in the interior of the formations [Figs. 6(a)–6(e)]. However, significant wake-wake and wake-cylinder interactions as well as faster bleeding flows between the middle and trailing rows, lead to higher TKE in the downstream of these formations. As ϕ increases to nonoverlapping cases, faster flow in the interior of the array and increased space allow wakes to become turbulent, resulting in TKE levels similar to isolated cylinder in wakes of all the formation members.

Below we describe the key characteristics of the formations by dividing them into three groups with the most similar patterns based on the experimental observations as discussed earlier. We will focus on the shear layers of each body (attached and detached) and how the shear layers, bodies, and wakes interact with each other. We will also explore how these interactions lead to changes in the frictional and pressure contributions to the drag force, and the asymmetries observed.

1. Most overlapping formations, ϕ = 22.6° and 27.6°

The leading members of formations with $\phi = 22.6°$, and 27.6°, shown in Figs. 3(a) and 3(b) and 4(a) and 4(b), experience wakes that partially encompass members 2 and 3, leading to wider

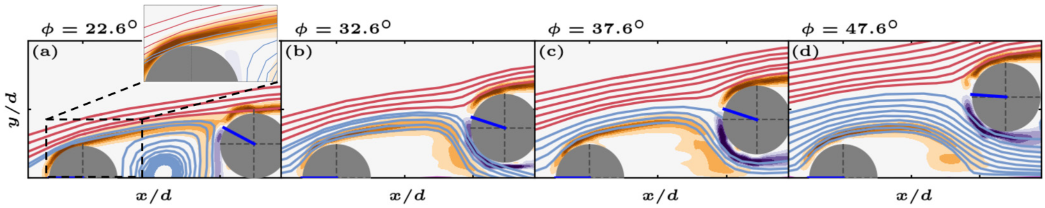

FIG. 7. Intersection of shear layers (colored vorticity contours) with the streamlines Int 1,2 and Int 2,4 for formations with (a) $\phi = 22.6°$, (b) $\phi = 32.6°$, (c) $\phi = 37.6°$, and (d) $\phi = 47.6°$, zoomed in from Fig. 5. The dark blue lines inside the cylinders, connecting the centers of the cylinders and their circumferences, denote the location of the frontal stagnation points.

wakes in the normal (y) direction compared with the solo case. For these lowest angles, only a small amount of flow enters the interior of the formation, and the magnitudes of the equivalent bleeding flows, U^b_{12} and U^b_{13}, are limited to less than about $0.09U_\infty$. In parallel, the normal velocity between members 1-2-3 exceeds that seen in the wake of the solo cylinder. Especially for the $\phi = 22.6°$, where members 2 and 3 are in contact, the wake consists of one extremely slow circulation (vortical) zone within the separation bubble [Fig. 5(a)], with the bleeding flow $\boldsymbol{u}^b_{12}$ entering the space and the bleeding flow $\boldsymbol{u}^b_{13}$ exiting. These wake-body interactions exhibit distinct differences compared with the dynamics of the Narrow formations previously discussed [41] and those of the intermediate overlap discussed in the upcoming Sec. III B 2.

The color-coded streamlines in Fig. 5(a) show that for $\phi = 22.6°$, the limited physical separation between members 1-2-3 (especially 2-3) significantly regulates the bleeding flows. This is clear from the limited normal (y) extent of the streamlines Int 1,2 and Int 1,3. These streamline groups, lie within the shear layers that are detached from the external sides of member 1, but they do not cover the full thickness of the shear layer and a portion of the streamline groups Int 2,4 and Int 3,5 fill the rest of the shear layers' thickness as shown in Fig. 7(a) and the inset where Int 2,4 streamlines pass through the shear layer as marked with the faded orange region of the vorticity contour. The detached shear flow from exterior of member 1 is divided into two streams at the stagnation points of members 2 and 3. A similar pattern occurs for $\phi = 27.6°$ where the exterior shear layers are mainly captured by Int 1,2 and Int 1,3 but only a marginal portion by Int 2,4 and Int 3,5.

In the $\phi = 22.6°$ formation, streamlines Int 1,2 enter the space between members 1-2-3 from the opening between members 1 and 2, from a separation bubble with one recirculating region, exit from the opening between members 1 and 3, reenter the interior of the formations through the space between members 3 and 5, and form a second recirculation zone in the separation bubble behind member 3. Int 1,3 also enters via the opening between members 1 and 3, and gets contained in the separation bubble. On the other hand, the portion of the shear layers which coincide with portions of the Int 3,5 and Int 2,4, flow on the exterior of members 2 and 3 and turn into the shear layers that detach from the exteriors of these two members [Fig. 5(a)]. This pattern resembles the "shear flow reattachment" observed for two cylinders in staggered configurations with center-to-center distances less than three diameters and side angles less than 10°–20° [44]. While Int 2,4 turns into the shear layer that detaches from the wall of member 2, both Int 1,2 (that exits the space between 1-2-3) and Int 3,5 together become the shear layer detaching from exterior of member 3. Therefore, only in the small region of the external attached shear layers, members 2 and 3 are exposed to flow with speeds on the order of U_∞, leading to higher velocity gradients and shear stresses at the wall. The remainder of the perimeter of the cylinders experience lower velocities and shear stresses. This results in cylinders 2 and 3 to experience lower average shear stresses compared with a single cylinder. However, due to the asymmetry of the flow, member 3 is largely encapsulated by Int 1,2 streamlines while member 2 is exposed to the faster shear layers (Int 2,4).

Between members 2 and 3 of the $\phi = 27.6°$ formation, the bleeding flow $\boldsymbol{u}^b_{23}$ causes the flow to be more attached to member 3 than member 2 and leading to a larger wake and separation bubble behind member 2. This results in a larger pressure contribution to the drag of member 2 and to uneven drag coefficients between members 2 and 3. For this angle, Int 2,4 streamlines lie at the edge of the shear layers where vorticity vanishes and this portion of the shear layer of member 1 reattaches to members 2 and 3. As the formation angle increases, separation between members 1 and 2 enables an increase in the bleeding flows $\boldsymbol{u}^b_{12}$ and $\boldsymbol{u}^b_{13}$. With a slight gap between members 2 and 3 for the case of $\phi = 27.6^\circ$ [Figs. 3(b) and 4(b)] the equivalent bleeding flows U^b_{12} and U^b_{13} are substantially higher (∼9%) with the two bleeding flows merging into $\boldsymbol{u}^b_{23}$. However, the limited space does not change the pattern compared with $\phi = 22.6^\circ$ and a single recirculating vortex remains in the separation bubble between cylinders 1-2-3 [Fig. 5(b)] and, again, Int 1,2 streamlines enter the separation bubble, create the recirculating region, and, this time, exit via the gap between members 2 and 3. The Int 1,3 streamlines enter the bubble and are trapped in the recirculation. The Int 1,2 streamlines exit and join the recirculating region in the separation bubble behind member 3.

In the $\phi = 27.6^\circ$ formation, however, streamlines remain attached to member 3 (Int 1,2 from one side, Int 1,3 from another, and Int 3,5 from the exterior side) for a larger portion of the perimeter than member 2 [Fig. 5(b)]. The flow detachment in the downstream of member 2 results in a larger contribution of pressure drag relative to member 3 causing a large disparity in the $C_{D,2}$ and $C_{D,3}$ [Fig. 2(a)]. Due to the described asymmetry, for both $\phi = 22.6^\circ$ and 27.6°, member 2 exhibits a more defined, frontal stagnation point than member 3 leading to member 2 experiencing a greater momentum transfer and higher drag force than member 3 (Fig. 2). This asymmetric flow pattern, in general, results in different drag coefficients for members within the same row (2, 3 or 4, 5).

For members 4 and 5, increase in the spacing in the normal (y) direction (compared with members 2 and 3) results in slightly larger bleeding flows (U^b_{24} and U^b_{35}, both less than $0.27U_\infty$) into the interior of the formations. These two bleeding flows combine to form the $\boldsymbol{u}^b_{45}$ bleeding flow between members 4 and 5. Due to the asymmetry of the flow field and the difference in the magnitudes of U^b_{24} and U^b_{35}, the direction of the $\boldsymbol{u}^b_{45}$ is dictated by the bleeding flow with larger momentum, resulting in a large disparity between the wakes of the members 4 and 5 for these two formations. For example, Figs. 4(a) and 5(a) show a larger region of negative normal velocity past member 4 and 5 of $\phi = 22.6^\circ$ formation, and streamlines that encompass member 5, move away from member 4 of the $\phi = 22.6^\circ$ formation. The reverse of this pattern is seen for $\phi = 27.6^\circ$ where Figs. 4(b) and 5(b) show a large region of positive normal velocity past member 5 toward the wake of member 4 and thus the streamlines constricting the wake of member 4. In other words, the bleeding flow with the larger velocity magnitude (and thus momentum) dictates the distribution of the shear layers around the bodies. This causes a more detached flow for the body adjacent to the streamline while bending the other streamline to get more attached to the other member of the same row. For example, with $U^b_{24} > U^b_{35}$ in the $\phi = 22.6^\circ$ formation, member 4 exhibits a more detached flow while the flow around member 5 stays attached, This results in member 5 experiencing a pressure recovery downstream and a lower drag force than member 4. Conversely, for the $\phi = 27.6^\circ$ formation where $U^b_{35} > U^b_{24}$, flow past member 4 remains more attached while member 5 exhibits detachment, leading to member 4 experiencing a pressure recovery downstream and thus a lower drag force than member 5 (see Sec. III C). Therefore, it is the dynamics of the shear layers in the bleeding flows, their attached and detached behavior, and their interactions with each other and the wakes, that clearly regulate the bleeding flows as a whole and ultimately lead to a combined reduction in the pressure and friction drags experienced by the members.

The confined space between members 1-2-3 for both formations also affects the turbulence statistics of the wake. At $\mathrm{Re}_d = 1,100$ the wake of a solo cylinder becomes turbulent with a formation length of $\approx 2.6d$ (as shown in Fig. 6). But for members 1, 2, and 3 of these two formations, the TKE of the wake remains near zero with traces of nonzero TKE visible only in the wakes of the trailing members.

Lastly, the asymmetry about the $y = 0$ line or between members of the same row, especially between members 2/3, and 4/5, of the five-cylinder system, has partial similarities to bistable behavior of three-cylinder fluidic pinball systems (three cylinders of same diameter forming a ∨ formation as an equilateral triangle). These systems undergo a pitchfork bifurcation when the center-to-center spacing is below ∼2.3 times the diameter of a single cylinder [84–88]. As a result of this bistability, the bleeding flow between the trailing cylinders does not stay symmetric and gets deflected toward one side (see sensitivity analyses by Noack *et al.* [86] and Deng *et al.* [87,88]). Similar asymmetric wake fields, that are biased toward one cylinder, occur in flows past side-by-side cylinders at "intermediate" separations of 1.1–2.2 diameters [44,45,49]. In all cases, the bleeding (or gap) flow is deflected and asymmetry persists until separations exceeds 2.2 times the diameter. Although additional members complicate the wake-wake interactions, the similarities with the fluidic pinball and the side-by-side cylinder experiments warrant future statistical investigation into flow stability and sensitivity analysis for formations with smaller ∨ angles, which is beyond the scope of this work.

2. *Intermediate overlaps,* $\phi = 32.6°–47.6°$

For the remaining formations with overlaps ($\phi = 32.6^\circ$, 37.6°, 42.6°), and the marginal case of $\phi = 47.6^\circ$, increasing the space between members 2 and 3, increases the bleeding flow into the interior of the formation. Unlike the negligible bleeding flow $\boldsymbol{u}_{23}^{b}$ of $\phi = 22.6^\circ$ and 27.6°, starting from the $\phi = 32.6^\circ$ the bleeding flow between members 2 and 3 gradually establishes symmetry between the upper and lower echelons [Figs. 3(c)–3(f), 4(c)–4(f), and 5(c)–5(f)] and the differences between flow patterns around members 2 and 3, and members 4 and 5 diminishes as the angle increases. In the wake of member 1, two recirculating regions form in the separation bubble between members 1-2-3 which are fully enclosed by the streamline groups of Int 1,2 and Int 1,3 [Figs. 3(c)–3(f), 4(c)–4(f), and 5(c)–5(f)]. These two streamline groups flow into the interior of the formations, bending inward at the stagnation points on members 2 and 3. In the case of $\phi = 32.6^\circ$, the wake of member 1 shifts the two stagnation points compared to the position of the stagnation point of the solo cylinder (see the dark blue lines inside the cylinders in streamlines figures of Fig. 5). Thus, the thickness of the wake of member 1 stays slightly larger than the solo case and larger than the nonoverlapping cases (Sec. III B 3). As the angle is increased and with larger space, streamlines Int 1,2 and Int 1,3 narrow the width of the wake of member 1 and the stagnation points of members 2 and 3 slowly return to the single cylinder reference location. These two streams also limit the horizontal extent of the wake to slightly less than $2.5d$ (compared with close to $3.5–4d$ for the solo cylinder).

Similar to the most overlapping formations (Sec. III B 1), attached shear layers on the interior of the formation with lower speeds, and limited attached shear layer on the exterior, with speeds on the order of the U_∞, result in lower frictional contribution to the drag forces. Here the streamline groups Int 1,2 and Int 1,3 are part of the two shear layers detached from member 1 [Figs. 7(b) and 7(c)] that bend inward at the stagnation points of member 2 and 3 to turn into bleeding flows $\boldsymbol{u}_{12}^{b}$ and $\boldsymbol{u}_{13}^{b}$ in the interior of the formation. However, streamline groups Int 2,4 and Int 3,5 lie outside of the boundary layers of member 1. Therefore, for this group, Int 2,4 and Int 3,5 are only part of the shear layers detaching from members 2 and 3 [Figs. 7(b) and 7(c)] and with the shift in the stagnation points and clear separations happening close to 90°, these streamlines remain attached to members 2 and 3 for $\lesssim 25\%$ of the circumference. On the other hand, the shear layers detached from member 1 [Figs. 5(c)–5(f) and 7(b) and 7(c)], reattach to the interior of members 2 and 3, and remain attached over a larger portion of the inner circumference due to the limited space between the two cylinders. With the exterior shear layers having faster velocities outside the boundary layer comparable to that of the solo cylinder, and the shear layers on the interior having slower speeds, members 2 and 3 of these formations experience lower levels of shear stress on average compared with the solo cylinder and this contributes to the lower drag forces experienced by the members compared with the solo reference. As the formation angle increases, the magnitudes of the bleeding flows increase, the shear stress on the interior is also expected to increase, thus increasing the drag force of the same member (Fig. 2).

For formations with intermediate overlaps, increasing the formation angle makes the flow field more symmetric about the $y = 0$ line. Cases with $\phi = 32.6^\circ$ and 37.6° maintain the highest asymmetry between the two echelons (members 2/3, and 4/5) as is seen in the drag coefficients (Sec. III A) and the wakes and streamlines [Figs. 3(c) and 3(d), 4(c) and 4(d), and 5(c) and 5(d)]. Focusing on members 2 and 3, the asymmetry of the streamlines around each of the bodies leads to the flow field to be more attached to one of the cylinders and more detached from the other one. For example, for both $\phi = 32.6^\circ$ and $\phi = 37.6^\circ$, member 3 experiences a more attached flow (where Int 1,3 encloses the body). This results in less pressure contributions to the drag of member 3 compared to member 2, resulting in a lower total drag force experienced by cylinder 3 (cumulative with the friction drag similar to the discussion in the previous Sec. III B 1). For both these cases with the magnitude of the U_{23}^b bleeding flow increasing (see Tbl. SM.1 in the Supplemental Material [83]), the drag force is larger than the lowest values recorded for $\phi = 22.6^\circ$ and $\phi = 27.6^\circ$. Starting from $\phi = 42.6^\circ$, the two echelons become more symmetric where the streamlines around members 2 and 3 of $\phi = 42.6^\circ$ and $\phi = 47.6^\circ$ becoming nearly symmetric, thus eliminating the difference between the C_D of members 2 and 3. Ultimately, between members of the same row, the member with a larger interior attached shear layer (lower velocities) and smaller wake, experiences the lower drag between the two, where the smaller wakes reduce the pressure contribution to the drag.

Streamlines Int 2,4 and Int 3,5 past members 4 and 5 that are moving into the formation, have a similar pattern as streamlines Int 1,2 and Int 1,3 past members 2 and 3 moving into the formation. Streamline groups Int 2,4 and Int 3,5 are part of the detached shear layers from members 2 and 3, which reattach to members 4 and 5 on the inside as part of the $\boldsymbol{u}_{45}^b$ bleeding flow, while streamline groups Ext 4 and Ext 5 bypass the upstream shear layers and only pass through the exterior shear layers detached from members 4 and 5. Besides the blockage caused by the group of bodies, theses streamlines experience no restrictions and closely resemble the streamlines past the single member case. Ext 4 and Ext 5 are only in contact with about $\lesssim$25% of the circumference. On the other hand, Int 2,4 and Int 3,5 pass on the interior and are faster than the streams past members 2 and 3 due to the increased spacing. Therefore, members 4 and 5 experience larger shear stress and friction drag compared with members 2 and 3. In addition, Figs. 5(c)–5(f) reveal more attached streamlines around member 4 of the $\phi = 32.6^\circ$ (following Int 2,4) and member 5 of the $\phi = 37.6^\circ$, $\phi = 42.6^\circ$, and $\phi = 47.6^\circ$ (follow Int 3,5). This asymmetry reduces the pressure contributions to the drag for these members compared to the other member in the same row. Therefore, member 4 of the $\phi = 32.6^\circ$ has a lower drag force compared to member 5, and for $\phi = 37.6^\circ$ through $\phi = 47.6^\circ$, we see the reverse, where member 5 records a lower drag force compared to member 4.

Lastly, increasing the inter-member gap increases the TKE in the wakes of the bodies in the interior of the formation [Figs. 6(c)–6(f)], especially for members 2 and 3, which was absent in the most overlapping cases. Only for $\phi = 47.6^\circ$, nonzero TKE levels appear in the wakes of member 1 prior to the position of members 2 and 3; for higher angles, TKE levels approach the maximum value reported in the wake of the solo cylinder case. While the maximum values of the TKE are lower than that of the solo cylinder case, due to the limited space for the wake development for members 2 and 3, the formation lengths behind these cylinders are shorter than the solo cylinder case.

3. Nonoverlapping formations, ϕ = 52.6°–67.6°

For all the cases with $\phi \geqslant 52.6^\circ$ (no overlaps in the streamwise direction), we see the width of the wake of member 1 is smaller than the previous two groups [see Figs. 3(g)–3(j) and 4(g)–4(j)], as the space between members 2 and 3 allows larger bleeding flow magnitudes. Right before members 2 and 3, the normal velocity has a larger magnitude (especially on the interior sides) than the solo cylinder case. Similarly, we can see in Figs. 5(f)–5(i) the streamlines on either side of each of the bodies divide upstream of the member at the stagnation points, go around the bodies, and rejoin downstream, enclosing the bodies, their wakes, and the separation bubbles inside a fictitious boundary. For example, similar to the formations with intermediate overlaps, the streamline groups Int 1,2 and Int 1,3 completely encompass member 1, its wake, and separation bubble, before the centerlines of members 2 and 3 (within 2.5d). Similarly, Int 1,2 and Int 2,4, and Int 1,3 and Int

3,5 separate at the stagnation points of members 2 and 3 and rejoin before members 4 and 5, fully enclosing members 2 and 3 and their wakes and separation bubbles. The physical size of these bounding regions around members 1, 2, and 3 and their wakes, are markedly smaller than the boundary around the solo cylinder, due to the continuity dictating the existence of the bleeding flows $\boldsymbol{u}_{23}^b$ and $\boldsymbol{u}_{45}^b$, between members 2-3 and 4-5. As a result, the streamlines are forced to be closer to the bodies, and bend and join together at an earlier distance compared with the single cylinder case. This results in shear layers separating at a slightly later point along the circumference of the bodies at angles larger than 90° compared to the usual 80°–85° separation points seen in the solo cylinder cases [64]. While this slightly increases the frictional drag force, it mostly helps with the pressure drag on the body which results in the leading member experiencing a lower drag force even at the largest ∨ angles and a 5%–8% drag reduction for members 2 and 3 of $\phi = 52.6^\circ$ and 57.6°. Overall, while all the nonoverlapping cases here show almost similar behavior, the smaller angles of the group, especially that of the $\phi = 52.6^\circ$ and $\phi = 52.6^\circ$ can still offer benefits to three out of the five members of the group and can be effectively used in a formation design. Lastly, the limited length of the wake for members 1, 2, and 3 also impacts the development of the TKE in the interior of the formation [see Figs. 6(g)–6(j)], reducing the vortex formation lengths (location with the largest turbulent kinetic energy [42,57–59]) compared to the solo cylinder case.

While the wake of member 1 is nearly symmetric about its horizontal centerline, members 2–5 still experience asymmetries about their local horizontal centerlines ($y = y_c$) due to differences in the streams on the interior and exterior sides [Figs. 5(g)–5(j)]. Additionally, members of the two echelons (2 and 4, against 3 and 5) exhibit asymmetries about the global horizontal direction ($y = 0$ line). However, as the formation angle increases, the symmetry about $y = 0$ becomes stronger. These asymmetries are visible in Figs. 3(g)–3(j), where the wakes of the members have curved, asymmetric teardrop shapes. The asymmetry in the flow past either cylinder 2 or 3 is also seen in the normal velocity distribution in Figs. 4(g)–4(j); the streamlines of the bleeding flows $\boldsymbol{u}_{23}^b$ on the interior side flow straight toward the space between members 4 and 5 and join the bleeding flow $\boldsymbol{u}_{45}^b$, while the exterior streamlines bend inward and shape the bleeding flows $\boldsymbol{u}_{24}^b$ and $\boldsymbol{u}_{35}^b$. The trailing members 4 and 5, which have unobstructed space downstream, develop wakes more similar to the wake of a solo cylinder (but with the noted asymmetries).

Even with the differences in the flow field and the streamlines, members 4 and 5 of these formations record similar drag values as solo cylinder (Fig. 2). For members 4 and 5 in wider formations, the larger intermember spacing leads to the bleeding flows to develop without forcing the streamlines to move closer to each other. Hence, for $\phi \geqslant 57.6^\circ$, the drag coefficients of members 4 and 5 return to that of the solo cylinder case; even member 5 recording slightly higher drag. Overall, the drag forces for most interior and trailing members are similar and especially for the $\phi = 67.6^\circ$, the drag force experienced by most of the members approaches the drag force of a single cylinder reference.

C. Local view of the flow field around each member

To further compare the effect of formation angles on each cylinder, we change our point of view from the global coordinate system at the center of cylinder 1, to a local coordinate system attached to the center of each member [denoted by (x_c, y_c)], and present the velocity and pressure fields as seen by a specific member in the upstream and downstream positions across different formations (ϕ). We focus on how each member experiences the velocity and pressure fields upstream and downstream, and compare them against the rest of the members and the solo cylinder reference case, and ultimately connect the results to the global view discussed in Sec. III B.

The velocity profiles upstream of each member (Fig. 8) experience large variations as a function of the formation angle, compared to the profiles on the downstream side (Fig. 9). Among the cylinders, for all members of the interior and trailing rows (2–5), velocity fields recorded at $1.25d$ upstream of each member [Figs. 8(b)–8(e)] show large differences as the formation is changed and when compared with the single cylinder case (shown with black dashed lines). It is only for the

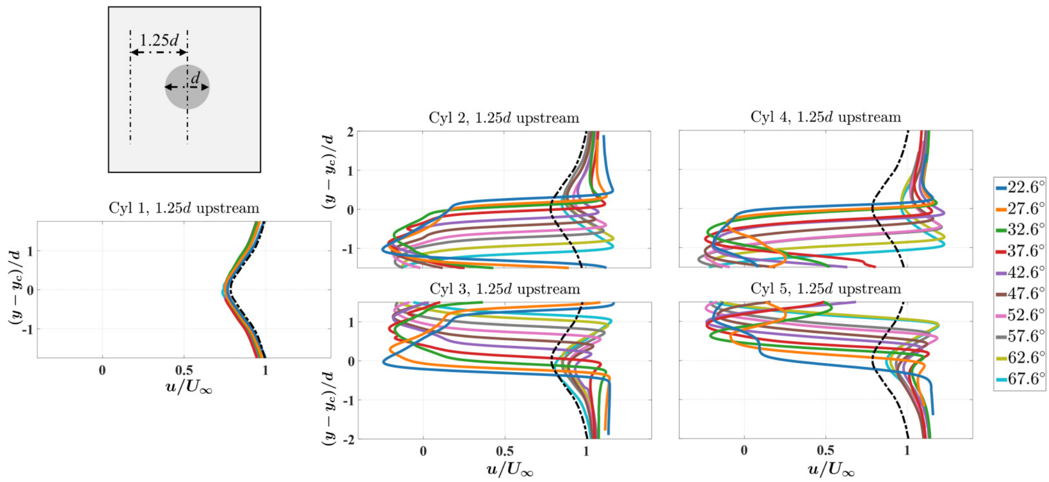

FIG. 8. Streamwise velocity profiles, u/U_∞, 1.25d upstream of the center of the members, plotted with respect to the center of the member as shown in the top left schematic. Black dash-dotted line represents the velocity at $x/d = 1.25$ upstream of a single cylinder. An expanded view of the figure is presented in Fig. SM.3 in the Supplemental Material [83] Sec. SM.C.

leading member [Fig. 8(a)] that upstream velocity profiles nearly collapse on each other. Due to the presence of multiple bodies in the path of the flow (as reported previously [41]), the upstream velocity of all the formations is slightly lower than that of the reference solo cylinder case.

The upstream differences seen by the rest of the members (interior and trailing, 2–5) result directly from variations in the formation angles, and mostly appear as similar profile patterns with transverse shifts in the y direction with respect to each other. As discussed previously [41], within a formation of nonlifting bodies, three phenomena dictate the flow dynamics around the members: (1) the wake of the upstream members, (2) the stagnation points of the downstream members, and (3)

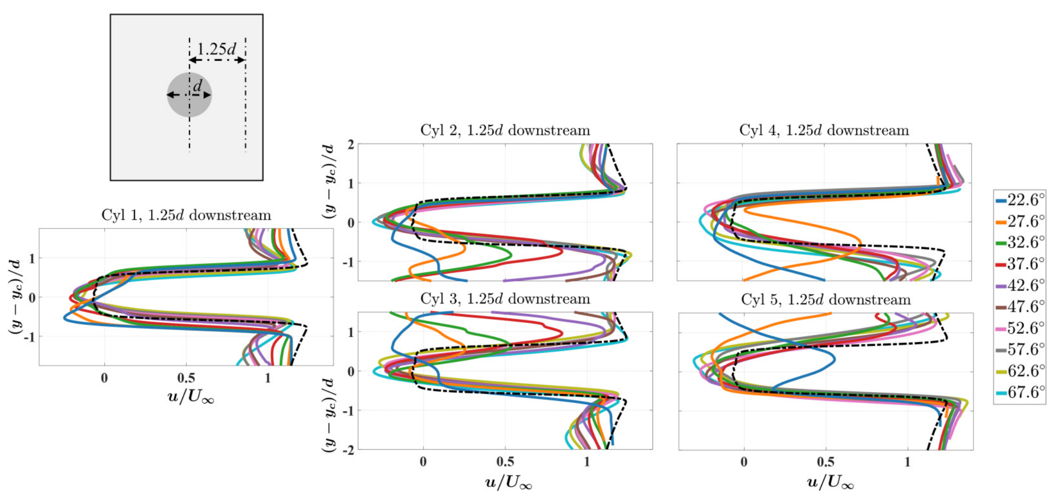

FIG. 9. Streamwise velocity profiles, u/U_∞, 1.25d downstream of the center of the members, plotted with respect to the center of the member as shown in the top left schematic. Black dash-dotted line represents the velocity at $x/d = 1.25$ downstream of a single cylinder. An expanded view of the figure is presented in Fig. SM.4 in the Supplemental Material [83] Sec. SM.C.

the bleeding flow between two members. Focusing on the widest angle here, $\phi = 67.6^\circ$, these three phenomena are seen as three separate regions in the velocity profiles of cylinders 2–5. The wake deficit is the largest slow-down region in the profile, bleeding flows correspond to the speed-up regions ($u/U_\infty > 1$) that limit the lateral extent of the wake in y direction, and a smaller region of slow-down (velocity magnitude) due to the impact of the upcoming body and stagnation point. Similarly, these three regions are easily distinguishable in the nonoverlapping cases with $\phi > \phi^*$, but as we reduce the formation angles, the separation between the three regions shrinks and the distinction between the bleeding flow and the slow down due to stagnation becomes less clear. Especially in overlapping cases, $\phi < \phi^*$, where the upstream wake impacts the $-0.5d < y - y_c < 0.5d$ (immediate frontal view), the velocity profile is dominated by the wake deficit, with only dilute effects from bleeding flow and upcoming stagnation points visible. As seen from the dark blue lines marking the locations of stagnation points on each body in the streamline plots of Fig. 5, as ϕ decreases, the location of the stagnation point is pushed outward relative to the 180° horizontal angle of the stagnation point of the solo cylinder case. For larger ϕ angles, we see the locations of the stagnation points slowly return to the same position as that of the solo cylinder, but flow past the members maintains an asymmetry due to the geometric constraints between two side-by-side members. This also contributes to the stagnation points appearing as smaller slow-down regions upstream of the cylinders for all $\phi \geqslant 37.6^\circ$ formations, as seen in Fig. 8. For overlapping formations, such as $\phi = 42.6^\circ$, $\phi = 37.6^\circ$, and $\phi = 32.6^\circ$, the stagnation slow-down follows the outward shift discussed in Sec. III B 2, and also seen in Fig. 8. For $\phi = 22.6^\circ$ and 27.6° the slow-down due to the stagnation point is much more dilute for members 2 and 3, as the wake of member 1 encompasses members 2 and 3 as discussed in Sec. III B 1. As the angle increases, the location of the slow down moves closer to the $y = y_c$, similar to the reference solo cylinder (black dashed line).

The wakes of upstream members play the largest role in dominating the velocity profiles upstream, compared with bleeding flow and the upcoming stagnation points [Figs. 8(b)–8(e)]. Comparing the velocity profiles upstream of the interior members 2 and 3 and the profiles of member 1 cross all formations, shows how upstream wakes alter the velocity distribution compared to only one upcoming stagnation point in the flow. The wakes are always located directly behind their respective members. Increasing the formation angle increases the transverse separation, y, of the valley of the velocity deficits with respect to the $y = y_c$ line, shifting them toward the interior of the formation with respect to the center of the upcoming member. Therefore, for nonoverlapping $\phi > \phi^*$ formations, the upstream wake moves away from the immediate view of the member ($-0.5d < y - y_c < 0.5d$ region), and it is dominated by the stagnation slow-down and the bleeding flow speed up. As the formation angle is increased, the velocity profiles asymptotically approach the profile of a solo cylinder, but as seen in Sec. III B, the separations tested here are not yet large enough to reach the point where all the cylinders are uninformed of each other's presence. As expected, the exterior sides of the profiles resemble the profile of the solo cylinder more than the interior sides. This asymptotic behavior is clearer for members of the middle row, 2 and 3. Members 4 and 5 of the trailing row experience a higher velocity in the exterior, mainly due to the blockage caused by the entire formation. For the most-overlapping $\phi = 22.6^\circ$ and 27.6° cases, a wide extent of the views of the members is covered by the upstream wakes and the streamlines of the bleeding flow that join the recirculating regions in the wakes. This blends the impacts of the bleeding flow, the upcoming stagnation points, and the wakes.

The dominance of the impact of the wakes on the flow field is clearer when focusing on the downstream velocity profiles (Fig. 9, viewing from the downstream side of the members). Since the wakes form immediately downstream of the bodies, the velocity profiles for the same member across different formations present closer similarities, with wake deficits nearly collapsing onto each other and the impacts of the bleeding flow and the stagnation points appearing only as differences toward the interior of the formations. As discussed in Sec. III B and seen in the profiles of Fig. 9, in formations with frontal overlaps ($\phi < \phi^*$), the width of the wake deficit in the downstream of the leading member is larger than in nonoverlapping formations ($\phi > \phi^*$). Due to the bleeding flows from either side of the cylinders, the valley of the wake deficits behind all the members

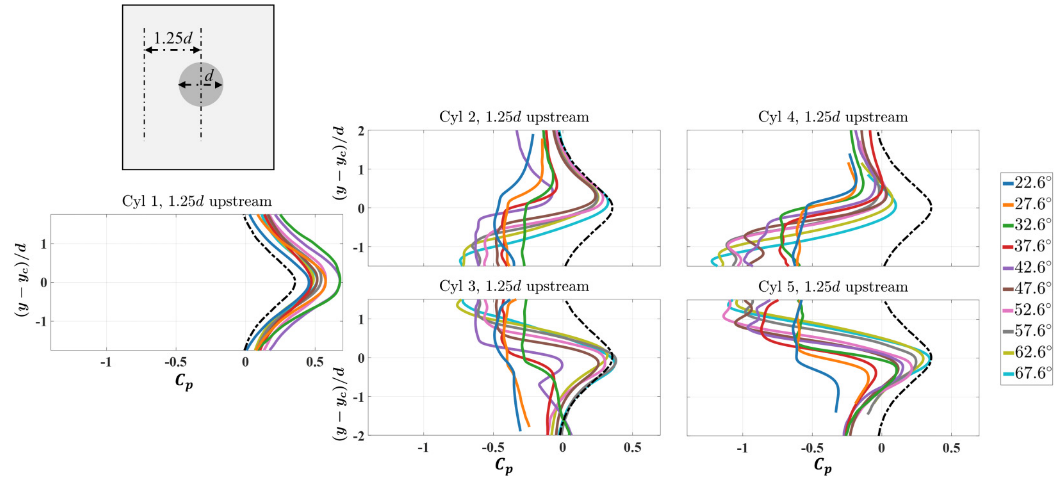

FIG. 10. Pressure coefficient profiles, C_p, $1.25d$ upstream of the center of the members, plotted with respect to the center of the member. Black dash-dotted line represents the pressure coefficient at $x/d = 1.25$ upstream of a single cylinder. An expanded view of the figure is presented in Fig. SM.5 in the Supplemental Material [83] Sec. SM.C.

present a sharper pattern compared with the blunt valley of the wake deficit of the solo cylinder. The bleeding flows alter the development of the wakes, leading to earlier spatial development of recirculating regions and the separation bubble than in the solo cylinder (see Figs. 3, 4, and 5) where larger negative u values appear in the wakes compared to the solo cylinder. Between all the cylinders, the members of the middle row (2 and 3) exhibit narrower wakes than trailing and leading members, independent of the formation angle. This is mainly due to the constraints of the bleeding flow imposed by the conservation of mass and the available geometric opening between the bodies. As a result, streamline groups Int 2,4 and Int 3,5 passing on the sides of members 2 and 3 are forced

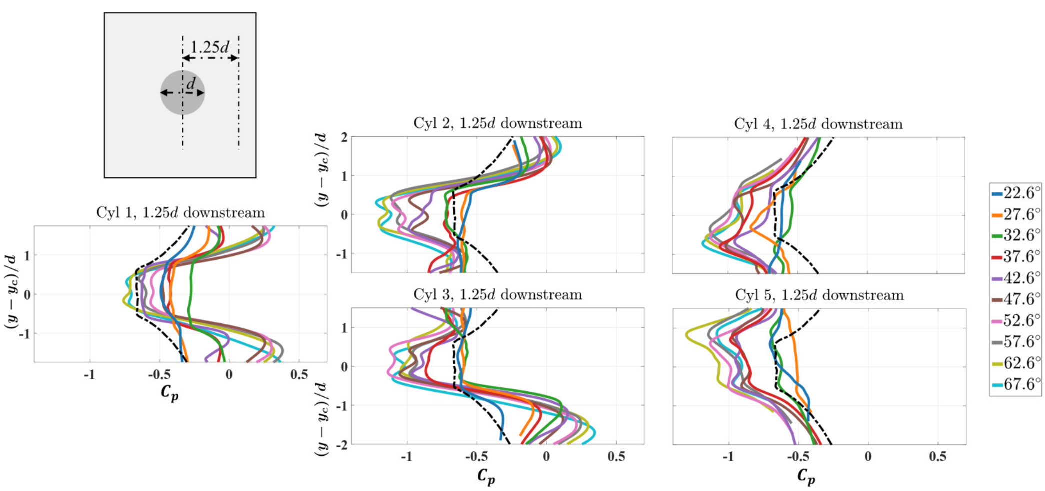

FIG. 11. Pressure coefficient profiles, C_p, $1.25d$ downstream of the center of the members, plotted with respect to the center of the member. Black dash-dotted line represents the pressure coefficient at $x/d = 1.25$ downstream of a single cylinder. An expanded view of the figure is presented in Fig. SM.6 in the Supplemental Material [83] Sec. SM.C.

through the opening between members 4 and 5, becoming part of the $\boldsymbol{u}_{45}^{b}$ bleeding flow. This is while members 4 and 5 have no downstream restrictions. These streamlines thus bound the flow and limit the development of the wakes of members 2 and 3 resulting in a narrower wake compared to the wakes of members 4 and 5 that are somewhat (but not fully) free to develop downstream compared with the single cylinder case.

For interior members 2 and 3, and in most formations with frontal overlaps ($\phi < 42.6^\circ$) the separation between the side-by-side wake deficits of the two members is insufficient for the bleeding flow [seen along the $(x - x_c) = 1.25d$] to fully recover to the U_∞ and this results in slight differences between the velocity fields as a function of the formation angles. Starting from $\phi = 42.6^\circ$, we see minimal variations between the velocity profiles for the same member in different formations. The same pattern holds for members 4 and 5 where only formations with $\phi \leqslant 27.6^\circ$ show clear difference between the velocity profiles due to the bleeding flow and the upcoming stagnation points, and formations with $\phi > 27.6^\circ$ exhibit similar velocity profiles as the formation angle is changed.

We also compare the distribution of pressure coefficient, $C_p = (p - p_\infty)/(0.5\rho U_\infty^2)$, as seen locally by each member in the upstream and downstream positions, shown in Figs. 10 and 11. The key difference in the pressure coefficients (compared with a solo cylinder) is in the pressure recovery occurring downstream of the formation members, where, on average, the difference between the pressure distribution upstream and downstream is lower than in the single cylinder case. For the leading member, the presence of multiple bodies downstream of the flow results in a slightly higher pressure coefficient in the upstream, while on the downstream values exceed those of the single cylinder case at all points along the $x = 1.25d$ line. In nonoverlapping cases, although a pressure recovery is visible away from the $y = y_c$ line, the pressure coefficient in the wake is similar to that of the solo cylinder case. Overall, the pressure recovery, combined with the wake and the bleeding flows around member 1, results in the leading member universally benefiting from its position in the formation.

Moving to members 2 and 3, the upstream pressure coefficient for overlapping cases with $\phi < \phi^*$ differ visibly from nonoverlapping cases, with nonoverlapping ones resembling the solo cylinder profiles on the external side of the formation at $y - y_c > 0.5d$ for member 2, and at $y - y_c < -0.5d$ for member 3. For all overlapping cases, and the interior of the nonoverlapping formations, some level of pressure drop occurs compared to the pressure distribution upstream of a solo cylinder. Here the pressure coefficient follows the pattern dictated by the wake of member 1 which is clearly distinct from the flow field upstream of a single cylinder. However, as the formation angle increases, the pressure coefficients on the external sides of members 2 and 3 begin to resemble those of a solo cylinder. Comparing upstream and downstream, the pressure coefficients of overlapping formations, experience a lower pressure drop (on average) compared with the nonoverlapping cases. Especially for $\phi \leqslant 42.6^\circ$ formations, the differences in the C_p of the upstream and the wakes of members 2 and 3 show lower drops than the pressure drop between the upstream and downstream of a solo cylinder. Since the key impact of the pressure on the drag lies in this difference between upstream and downstream, all the overlapping cases, plus $\phi = 47.6^\circ$, benefit from the pressure recovery that is possible due to the presence of upcoming members and their stagnation points. For formations with the largest overlaps, namely, $\phi = 22.6^\circ$, 27.6°, and 32.6°, pressure recovery, along with the flow attachment from the complex bleeding flow patterns described in Sec. III B, result in substantial levels of drag reduction for members 2 and 3 of these formations.

Moving to the trailing row, the upstream profiles of the pressure coefficients of members 4 and 5 is dominated by the wake of members 2 and 3, and showing clear differences from the single-member case (as expected). But, on the downstream, the profiles of pressure coefficient show closer similarity to the single cylinder case due to the lack of geometric restrictions to the wake development downstream. Similar to members 2 and 3, members 4 and 5 in overlapping formations experience a slightly larger pressure drop (between upstream and downstream positions) than the solo cylinder case. However, as discussed in Sec. III B 1, pressure recovery behind member 4 of the 22.6° formation and member 5 of the 27.6° formation along with the greater flow attachment around these members, results in lower drag forces than their side-by-side members in the same row. For nonoverlapping formations with $\phi \geqslant 57.6^\circ$ the pressure drops across members 4 and 5 closely resemble the solo cylinder case, leading to members 4 and 5 experiencing drag coefficients in the similar range of the solo cylinder, with member 5 even experiencing slightly higher values of drag as seen in Fig. 2 in Sec. III A.

D. Temporal characteristics and vortex shedding patterns

While the main focus of this work is on the drag force on the bodies as a performance metric for individual members and the group, the asymmetry in the flow field suggests the possibility of variations in the lift forces. In this section, we explore the potential for bodies to experience a nonzero lift force (force in the y direction) along with the frequency response of the vortex shedding. A single cylinder in flow experiences a steady state drag and zero steady state lift, but, the instantaneous vortex shedding behind the cylinder generates a temporal lift distributions that averages to zero in steady state conditions. Thus, cylinders are generally treated as nonlifting. However, the presence of additional members in a group and the asymmetry in the flow field and pressure, as discussed in Sec. III B and III C, raises the possibility of mild levels of lift force on the cylinders. Using the control volume analysis of Sec. II C, we can estimate the lift of bodies; for the cylinders experiencing the most asymmetry (like the ones in the middle and trailing rows of the most overlapping cases, $\phi = 22.6^\circ$ and 27.6°; see Figs. 3 and 4), we record the largest lift-to-drag ratios, with the ensemble-averaged lift forces being $\sim$10%–15% of the total net force. However, due to the low magnitudes of the lift captured, a measurement technique with higher resolution than what was used here is required to capture this force (such as higher resolution load cells).

Instead of focusing directly on the lift force, given the link between vortex shedding, circulation, and lift, we explore the temporal characteristics of flow around the members of ∨ formations, and calculate the circulation $\Gamma = \oint \boldsymbol{u} \cdot d\boldsymbol{\ell}$ along two chosen closed curves encompassing the upper and lower regions in the wake of the members ($y > y_c$ and $y < y_c$) and present the results as a function of time t in Fig. 12. Schematics of these integration regions are shown in top-left of the Fig. 12. The black dash-dotted lines in Fig. 12 correspond to the upper and lower circulations behind an isolated cylinder. $t_0 = 1/f_0$ denotes the vortex shedding time period for an ideal long circular cylinder, estimated from the literature on the Strouhal number [$\mathrm{St}_d = d/(t_0 U_\infty)$] variation with the Reynolds number (Re_d) [62]. For $\mathrm{Re_d} \approx 1100$, the corresponding Strouhal number is $\mathrm{St}_0 \approx 0.215$.

Figure 12 shows that the leading and interior members of the first two most overlapping formations ($\phi = 22.6^\circ$ and 27.6°) exhibit flat, nonperiodic variation in Γ in their wakes. This results from the trapped recirculation and wakes of the leading and interior members in the separation bubbles of these tight formations as discussed in Secs. III B and III C and visible in Figs. 5(a) and 5(b). For the $\phi = 22.6^\circ$, Γ variations in the wakes of members 2 and 3 on the interior side ("Cyl 2 lower" and "Cyl 3 upper" in Fig. 12) are identical, due to the overlapping closed integration curves. As ϕ increases, the wake behind the members have more room to develop further and shed, and we see larger variations in circulation owing to periodic vortex shedding. Nonoverlapping formations show larger amplitudes of oscillation in the circulation on the interior side of the formation (lower side of cylinders 2 and 4, and upper side of cylinders 3 and 5) compared with those on the exterior. Among the intermediate overlapping cases, formation with $\phi = 32.6^\circ$ shows minimal oscillation similar to the most overlapping cases, while from $\phi = 37.6^\circ$ forward the amplitudes of oscillation grow with similar patterns as that of the nonoverlapping cases. Starting from $\phi = 37.6^\circ$ and higher, the mean of the Γ_{upper} and Γ_{lower} for each member get close to each other and reach the circulation values of the single cylinder case, leading to minimal or no lift on the bodies. This is particularly the case for the trailing members of all formations with $\phi \geqslant 37.6^\circ$.

As mentioned above, the sum of the circulations from the upper and lower shoulders can give an indication of the lift force experienced by a member. For interior and trailing members (2–5) of formations with $\phi \leqslant 32.6^\circ$, the largest variations occur in the Γ calculated in the interior of the formation (lower for cylinders 2/4 and upper for cylinders 3/5). In these formations, inner shear

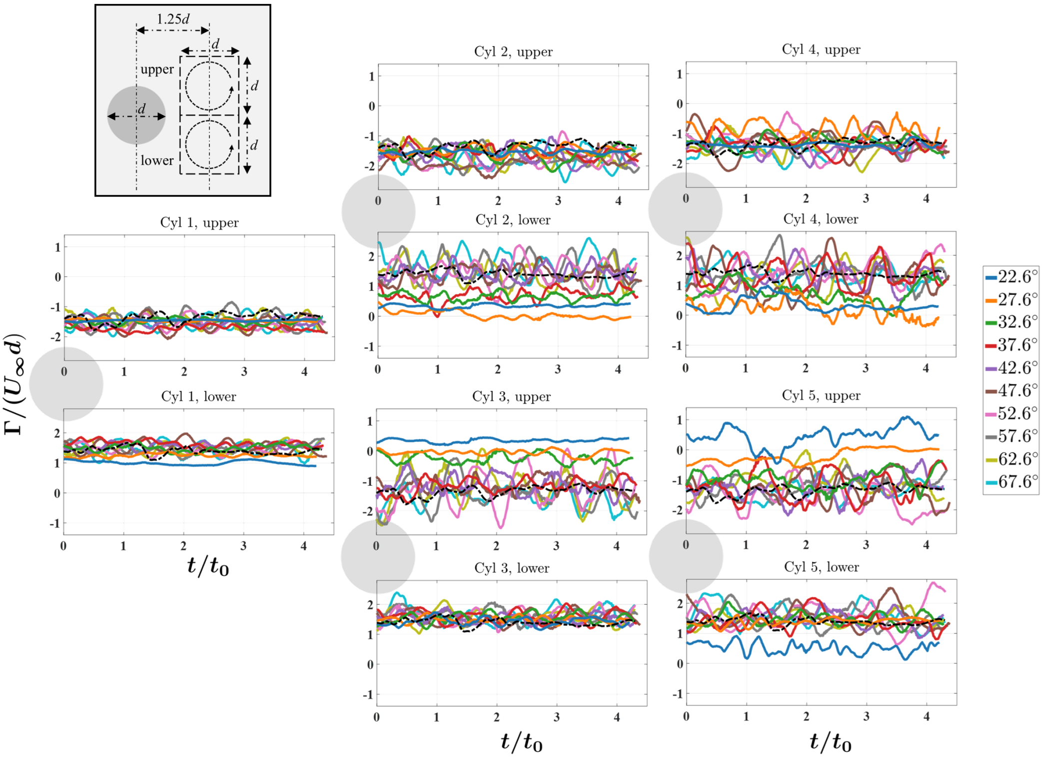

FIG. 12. Normalized instantaneous circulation, $\Gamma/(U_\infty d)$, as a function of nondimensionalized time, t/t_0, calculated in a $d \times d$ square region 1.25d downstream of the upper and lower shoulders (center of the square regions are downstream of the uppermost and lowermost points of the cylinder) of each cylinder for all the V formations (these square regions are shown on top-left of the figure). For visualization purposes, we use light gray circles to qualitatively denote the relative position of the formation members and connect the two plots of the upper and lower circulations for the same member. t_0 denotes the vortex shedding time period for an ideal long circular cylinder. The black dashed-dotted lines correspond to the upper and lower circulations due to vortex shedding behind a single, isolated cylinder. An expanded view of the figure is presented in Figs. SM.7, SM.8, and SM.9 in the Supplemental Material [83] Sec. SM.D.

layers of the members are controlled by the bleeding flow while outer shear layers are free to move and expand as needed (as discussed in Secs. III B and III C). Therefore, the averaged circulation magnitude (i.e. absolute value) on the outer shoulder is generally greater. For example, for cylinder 2, the average $\Gamma/(U_\infty d)$ from the lower (inner) shoulder for $\phi \leqslant 37.6^\circ$ formations is less than 1, while for the upper (outer) shoulder is around 1.5. This indicates the lift force experienced by cylinder 2 is in $+y$ direction (outward). Similarly, most members of these four formations with the largest recorded flow asymmetries (except the leading members) experience a small lift force (lateral force) in the outward direction (away from $y = 0$). However, these forces remain small compared to the streamwise drag forces (along $+x$ direction). Note that the variations in the phase of the plots are related to variations of the timing of consecutive-overlapping experimental data collections and the results have not been time-matched.

In addition to the average magnitude of the circulation (Fig. 12), the frequency of the vortex shedding is also impacted. To explore the temporal characteristics of vortex shedding, we present the frequency spectra of vortex shedding in Fig. 13, by taking the fast Fourier transform (FFT) of the time series of circulation presented in Fig. 12. The integral definition of the circulation serves as an average behavior of a region and is chosen over using a single point or few/many

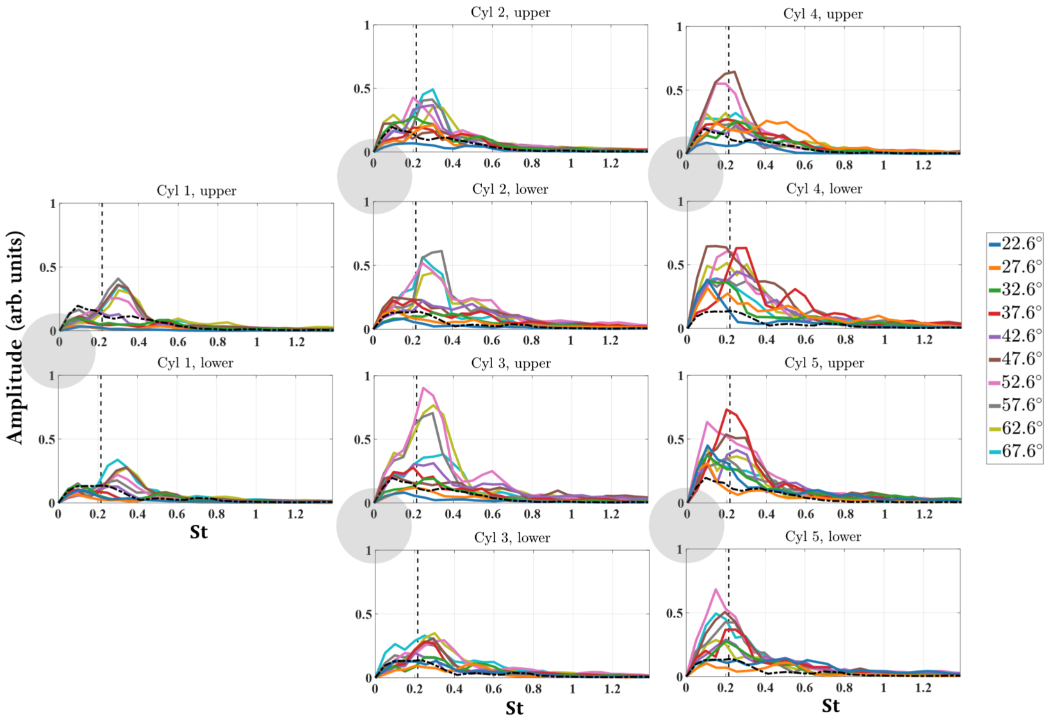

FIG. 13. Frequency spectra of the vortex shedding based on circulation, Γ, in a $d \times d$ square region $1.25d$ downstream of the upper and lower shoulders (center of the square regions are downstream of the uppermost and lowermost points of the cylinder) of each cylinder for all the $\vee$ formations. The dashed vertical black line indicates the shedding frequency for an ideal long circular cylinder. For visualization purpose, we use light gray circles to qualitatively denote the relative position of the formation members and connect the two plots of the frequency spectra of the upper and lower circulations for the same member. The black dash-dotted lines correspond to the frequency spectra of the vortex shedding (based on circulation) behind a single, isolated cylinder. An expanded view of the figure is presented in Figs. SM.10, SM.11, and SM.12 in the Supplemental Material [83] Sec. SM.D.

points in the wake. Frequency, f, is presented in the form of dimensionless Strouhal number ($\mathrm{St} = fd/U_\infty$). The dashed vertical black line indicates the shedding frequency for an ideal long circular cylinder.

For formations with small $\vee$ angles (most overlapping cases), significant interactions between the array members lead to irregular vortex shedding, leading to a more broad-band frequency response where, for members 1, 2, and 3, peak frequencies are obscured. However, trailing members 4 and 5, on the interior of the formation, show a peak frequency comparable to the single-cylinder case. Nonoverlapping cases display more pronounced frequency responses with increased shedding frequency on both interior and exterior sides of leading member 1, and interior members 2 and 3. Trailing members, however, exhibit lower shedding frequencies than other members, but the frequencies exceed that of the single cylinder case. The formations with intermediate overlaps show frequencies in between the two other groups, with combinations of both broadband responses and peak frequency increases depending on the asymmetry of the flow around each of the bodies.

While the main focus of this work has been on the impact of formations on drag force, the discussion presented here along with Figs. 12 and 13 demonstrate the potential of formations for tuning multiple flow characteristics beyond drag. Future works should explore the mechanisms driving the variations in the temporal flow response for individual members of the formation and the group as whole, the impact of the geometry of the formation on the frequency response and the lift forces, and consider these as part of the optimization process to be used for design of formations of uncrewed vehicles.

IV. CONCLUSIONS

As demonstrated here, ∨ formations are an effective way to control the flow field to tune the drag force of each member of a group and the entire formation. Over a wide range of formation angles, we see various levels of drag reduction, from substantial reductions as much as 78% (member 3 of the $\phi = 22.6^{\circ}$) in formations with overlaps in frontal views, to moderate reductions for formations with intermediate or no overlaps. At the chosen streamwise spacing (slightly less than formation length of a single cylinder), up to an angle of around 60°, we can achieve variations of drag reduction depending on the position of the member, for all (angles of less than 50°) or some of the bodies (angles between 50° and 60°). Beyond this angle, we only see the leading member experiencing a drag reduction. This knowledge offers a wide range of tunability for design of efficient formations depending on the application.

The sweep of the formation angles offers new insights into the dynamics of the flow field beyond what can be captured by the Narrow (overlapping) and Wide (nonoverlapping) designations [41]. The interactions of the flow between the members are a combination of wake-wake and wake-body interactions where the shear layers within the bleeding (or gap) flows play a key role in regulating these interactions. By separating the streamlines into groups according to their trajectories, we explore how the behavior of the shear layer attachment and detachment and the wake interactions modulate the pressure and friction drags of each member qualitatively which result in the quantitative drag values presented. We also show variations in the TKE within the wakes of all the bodies, compared with a solo cylinder, where formations with overlaps limit the transition to turbulence, while the nonoverlapping formations reach similar levels of TKE as that of the wake of a single cylinder.

The regulating nature of formations and their geometry is clearly visible in the variations in the velocity fields and pressure distributions between the members, as shown in the plots of velocity and pressure profiles upstream and downstream of each member in Sec. III C. In formations with overlaps, members can experience significant levels of pressure recovery which has a direct impact on the drag force experienced by the bodies. We also see that grouping the formations into three levels, based on their overlaps, allows us to describe the mechanism of the flow behavior in a more systematic manner; however, as shown, the borderlines between the groups are not fully fixed. Depending on the phenomenon of interest (drag, shedding, pressure field, etc.) the formation angles included in these groups can vary.

Additionally, pressure variations and the asymmetry between the top and bottom sides of each of the cylinders, especially leading and interior members (1, 2, and 3) of formations with overlaps, can also result in changes in the lift experienced by the body where varying levels of circulations are recorded in the wakes of each of the bodies. We also see potential in variations in the vortex shedding frequencies in the wakes of each of the members, especially for formation with no-overlaps.

Within the formation, the leading member experiences an interesting position. In our ∨ formations of nonlifting bodies, the leader's drag is minimized only in nonoverlapping cases relative to other group members. For overlapping cases, interior members experience the lowest drag relative to the entire group, while the leader experiences higher drag than interior members but still lower than a solo cylinder. Overall, the leader gains some benefit from formation compared to solo motion in all cases tested. A nonexhaustive review of the literature also reveals similar reports; for example, simulations of bird flocks (lifting bodies) based on incompressible aerodynamics and lift-induced upwash reveal a complex pattern. Most studies show that leaders gain some power reduction compared to solo flight, while followers experience greater power reduction [31,39]. Lissaman and Shollenberger [30] argue that the leading bird's position is not inherently the most strenuous, as any bird can adjust its drag through small position changes within the ∨ formation. A recent model of Northern Bald Ibis echelon formation flight shows that leading and trailing members experience approximately 30% drag reduction, while interior members experience 65%–70% reduction both compared to a solo bird [89]. Another report shows an 8% drag reduction for the leader and approximately 15% for the follower in a two-bird in-line flight compared to solo fliers [90]. Across other (nonlifting) animal locomotion models, leaders consistently show some level of benefit. For example, in diamond-shaped four-fish schools, the leader experiences about 1% to 4% drag reduction compared to a solo swimmer, with some scenarios where the leader experiences the least drag among all the fish [15], similar to the nonoverlapping cases here. In two-fish in-line swimming, leaders show about 2% to 3% drag reduction [16]. While more analysis is required to unify these observations, the majority of cases, including this work, suggest that nearly all members of a formation have the potential to experience a reduction in drag force. However, it is possible for the leading member to gain less benefit from this process than the rest of the members.

The results of this study provide a baseline for further investigation of wake-body and wake-wake interactions in flows past groups of bodies. It is clear that the choice of separation and orientation between the bodies has a direct impact on aero- and hydrodynamic performance in terms of drag and further work is required to clarify the impact of streamwise spacing on the drag forces experienced by the members; however, as briefly discussed, there is room for expanding the investigations to the temporal flow behavior and the potential for altering the lift forces of the bodies and the vortex shedding frequency, as well as considerations for the stability of the bodies, vortex-induced vibration, and the impact on the moments experienced by asymmetric bodies in groups. In addition, the similarities observed between asymmetric wake fields in tight formations with smaller angles, and fluidic pinball experiments and flow past side-by-side cylinders merit further experimental and theoretical investigations to study the stability of the flow past formations with tight ∨ angles and the impact of the stability on aero- and hydrodynamic loading on the bodies; this will be a subject for future work. While this work only offers insight into potential paths one can explore for tuning the drag of each member and the entire formation, ultimately, a combined understanding of all flow features impacted by formation geometry, including drag, lift, and temporal flow behavior will be required to inform formation designs needed to meet the objectives of aerial and underwater vehicles of interest along with the necessary considerations for safety and collision avoidance of vehicles in tight formations.

DATA AVAILABILITY

The data that support the findings of this article are not publicly available upon publication because it is not technically feasible and/or the cost of preparing, depositing, and hosting the data would be prohibitive within the terms of this research project. The data are available from the authors upon reasonable request.

[1] L. L. Gould and F. Heppner, The Vee formation of Canada geese, The Auk **91**, 494 (1974).

[2] R. M. May, Flight formations in geese and other birds, Nature (London) **282**, 778 (1979).

[3] C. Cutts and J. Speakman, Energy savings in formation flight of pink-footed geese, J. Exp. Biol. **189**, 251 (1994).

[4] H. Weimerskirch, J. Martin, Y. Clerquin, P. Alexandre, and S. Jiraskova, Energy saving in flight formation, Nature (London) **413**, 697 (2001).

[5] M. Nagy, Z. Ákos, D. Biro, and T. Vicsek, Hierarchical group dynamics in pigeon flocks, Nature (London) **464**, 890 (2010).

[6] S. J. Portugal, T. Y. Hubel, J. Fritz, S. Heese, D. Trobe, B. Voelkl, S. Hailes, A. M. Wilson, and J. R. Usherwood, Upwash exploitation and downwash avoidance by flap phasing in ibis formation flight, Nature (London) **505**, 399 (2014).

[7] A. Attanasi, A. Cavagna, L. Del Castello, I. Giardina, S. Melillo, L. Parisi, O. Pohl, B. Rossaro, E. Shen, E. Silvestri, and M. Viale, Collective behaviour without collective order in wild swarms of midges, PLoS Comput. Biol. **10**, e1003697 (2014).

[8] A. Cavagna, D. Conti, C. Creato, L. Del Castello, I. Giardina, T. S. Grigera, S. Melillo, L. Parisi, and M. Viale, Dynamic scaling in natural swarms, Nat. Phys. **13**, 914 (2017).

[9] J. F. Méndez-Valderrama, Y. A. Kinkhabwala, J. Silver, I. Cohen, and T. A. Arias, Density-functional fluctuation theory of crowds, Nat. Commun. **9**, 3538 (2018).

[10] J. C. Liao, D. N. Beal, G. V. Lauder, and M. S. Triantafyllou, Fish exploiting vortices decrease muscle activity, Science **302**, 1566 (2003).

[11] Y. Zhang and G. V. Lauder, Energy conservation by collective movement in schooling fish, eLife **12**, RP90352 (2024).

[12] H. Ko, G. Lauder, and R. Nagpal, The role of hydrodynamics in collective motions of fish schools and bioinspired underwater robots, J. R. Soc. Interface **20**, 20230357 (2023).

[13] S. Ito and N. Uchida, Vortex phase matching of a self-propelled model of fish with autonomous fin motion, Phys. Fluids **35**, 111902 (2023).

[14] J. Kelly and H. Dong, Effects of body shape on hydrodyanmic interactions in a dense diamond fish school, Phys. Fluids **36**, 031907 (2024).

[15] A. Menzer, Y. Pan, G. V. Lauder, and H. Dong, Fish schools in a vertical diamond formation: Effect of vertical spacing on hydrodynamic interactions, Phys. Rev. Fluids **10**, 043104 (2025).

[16] A. Menzer, Y. Pan, G. V. Lauder, and H. Dong, Fins in formation: Hydrodynamic impact of median fins in in-line fish swimming, Bioinspir. Biomim. **21**, 016013 (2026).

[17] R. G. Bill and W. F. Herrnkind, Drag reduction by formation movement in spiny lobsters, Science **193**, 1146 (1976).

[18] A. Kazemi, K. V. de Riet, and O. M. Curet, Drag coefficient and flow structure downstream of mangrove root-type models through PIV and direct force measurements, Phys. Rev. Fluids **3**, 073801 (2018).

[19] M. Gymnopoulos, A. M. Ricardo, E. Alves, and R. M. L. Ferreira, A circular cylinder in the main-channel/floodplain interface of a compound channel: Effect of the shear flow on drag and lift, J. Hydraul. Res. **58**, 420 (2020).

[20] A. Kazemi, L. Castillo, and O. M. Curet, Mangrove roots model suggest an optimal porosity to prevent erosion, Sci. Rep. **11**, 9969 (2021).

[21] M. Liu, W. Huai, B. Ji, and P. Han, Numerical study on the drag characteristics of rigid submerged vegetation patches, Phys. Fluids **33**, 08123 (2021).

[22] R. M. L. Ferreira, M. Gymnopoulos, P. Prinos, E. Alves, and A. M. Ricardo, Drag on a square-cylinder array placed in the mixing layer of a compound channel, Water **13**, 3225 (2021).

[23] F. He, H. An, M. Ghisalberti, S. Draper, C. Ren, P. Branson, and L. Cheng, Obstacle arrangement can control flows through porous obstructions, J. Fluid Mech. **992**, A3 (2024).

[24] A. T. Sayers, Flow interference between three equispaced cylinders when subjected to a cross flow, J. Wind Eng. Ind. Aerodyn. **26**, 1 (1987).

[25] G. Stanescu, A. J. Fowler, and A. Bejan, The optimal spacing of cylinders in free-stream cross-flow forced convection, Int. J. Heat Mass Transf. **39**, 311 (1996).

[26] R. Kumar and N. K. Singh, Three dimensional flow over elliptic cylinders arrays in octagonal arrangement, J. Thermal Eng. **7**, 2031 (2021).

[27] O. Yagci, O. Karabay, and K. Strom, Bleed flow structure in the wake region of finite array of cylinders acting as an alternative supporting structure for foundation, J. Ocean Eng. Mar. Energy **7**, 379 (2021).

[28] F. A. van den Brandt, S. G. Menting, F. J. Hettinga, and M. T. Elferink-Gemser, Drafting in long-track speed skating team pursuit on the ice rink, J. Sports Sci. **41**, 456 (2023).

[29] B. Blocken, T. van Druenen, Y. Toparlar, F. Malizia, P. Mannion, T. Andrianne, T. Marchal, G.-J. Maas, and J. Diepens, Aerodynamic drag in cycling pelotons: New insights by CFD simulation and wind tunnel testing, J. Wind Eng. Ind. Aerodyn. **179**, 319 (2018).

[30] P. B. S. Lissaman and C. A. Shollenberger, Formation flight of birds, Science **168**, 1003 (1970).

[31] D. Hummel, Aerodynamic aspects of formation flight in birds, J. Theor. Biol. **104**, 321 (1983).

[32] D. Hummel, The use of aircraft wakes to achieve power reductions in formation flight, *AGARD FDP Symposium on "The Characterisation & Modification of Wakes from Lifting Vehicles in Fluid", Trondheim, Norway, from 20-23 May 1996* (Advisory Group for Aerospace Research & Development (AGARD), North Atlantic Treaty Organization, 1996).

[33] W. Blake and D. Multhopp, Design, performance and modeling considerations for close formation flight, *23rd Atmospheric Flight Mechanics Conference* (AIAA, Boston, Massachusetts, 1998), p. 4343.

[34] D. Jacques, M. Pachter, G. Wagner, and B. Blake, An analytical study of drag reduction in tight formation flight, *AIAA Atmospheric Flight Mechanics Conference and Exhibit* (AIAA, Montreal, Canada, 2001), p. 4075.

[35] H. Kawabe, A study on optimal pattern and leader shift of formation flight, Trans. Japan Soc. Aero. Space Sci. **50**, 134 (2007).

[36] J. Xu, S. Andrew Ning, G. Bower, and I. Kroo, Aircraft route optimization for formation flight, J. Aircr. **51**, 490 (2014).

[37] S. A. Ning, T. C. Flanzer, and I. M. Kroo, Aerodynamic performance of extended formation flight, J. Aircr. **48**, 855 (2011).

[38] G. Bower, T. Flanzer, and I. Kroo, Formation geometries and route optimization for commercial formation flight, *27th AIAA Applied Aerodynamics Conference* (AIAA, San Antonio, Texas, USA, 2009), p. 3615.

[39] F. R. Hainsworth, Precision and dynamics of positioning by Canada geese flying in formation, J. Exp. Biol. **128**, 445 (1987).

[40] S. Guo, B. Alkouz, B. Shahzaad, A. Lakhdari, and A. Bouguettaya, Drone formation for efficient swarm energy consumption, in *2023 IEEE International Conference on Pervasive Computing and Communications Workshops and other Affiliated Events (PerCom Workshops)* (IEEE, 2023), pp. 294–296.

[41] P. Suchandra and S. Raayai-Ardakani, Impact of bio-inspired *V*-formation on flow past arrangements of non-lifting objects, Phys. Fluids **36**, 011909 (2024).

[42] C. H. K. Williamson, Vortex dynamics in the cylinder wake, Annu. Rev. Fluid Mech. **28**, 477 (1996).

[43] C. Williamson, Evolution of a single wake behind a pair of bluff bodies, J. Fluid Mech. **159**, 1 (1985).

[44] D. Sumner, S. Price, and M. Paidoussis, Flow-pattern identification for two staggered circular cylinders in cross-flow, J. Fluid Mech. **411**, 263 (2000).

[45] D. Sumner, Two circular cylinders in cross-flow: A review, J. Fluids Struct. **26**, 849 (2010).

[46] M. Zdravkovich and D. Pridden, Interference between two circular cylinders; series of unexpected discontinuities, J. Wind Eng. Ind. Aerodyn. **2**, 255 (1977).

[47] M. Zdravkovich, Review of flow interference between two circular cylinders in various arrangements, J. Fluids Eng. **99**, 618 (1977).

[48] M. Zdravkovich, The effects of interference between circular cylinders in cross flow, J. Fluids Struct. **1**, 239 (1987).

[49] Y. Zhou and M. M. Alam, Wake of two interacting circular cylinders: A review, Int. J. Heat Fluid Flow **62**, 510 (2016).

[50] D. Rockwell, Vortex-body interactions, Annu. Rev. Fluid Mech. **30**, 199 (1998).

[51] S. Fu, P. Suchandra, and S. Raayai-Ardakani, Multi-sheet illumination and consecutive overlapping 2D-2C PIV acquisition for enhanced access to boundary layer flows around obstructive opaque objects, in *Proceedings of the 15th International Symposium on Particle Image Velocimetry (ISPIV 2023)* (International Symposium on Particle Image Velocimetry, San Diego, 2023).

[52] A. Nair, A. Kazemi, O. Curet, and S. Verma, Porous cylinder arrays for optimal wake and drag characteristics, J. Fluid Mech. **961**, A18 (2023).

[53] N. Amini and Y. A. Hassan, An investigation of matched index of refraction technique and its application in optical measurements of fluid flow, Exp. Fluids **53**, 2011 (2012).

[54] S. F. Wright, I. Zadrazil, and C. N. Markides, A review of solid–fluid selection options for optical-based measurements in single-phase liquid, two-phase liquid–liquid and multiphase solid–liquid flows, Exp. Fluids **58**, 108 (2017).

[55] S. Fu and S. Raayai-Ardakani, Double-light-sheet, consecutive-overlapping particle image velocimetry for the study of boundary layers past opaque objects, Exp. Fluids **64**, 182 (2023).

[56] S. Fu and S. Raayai-Ardakani, Localised performance of riblets with curved cross-sectional profiles in boundary layers past finite length bodies, J. Fluid Mech. **1013**, A21 (2025).

[57] P. Bearman, Investigation of the flow behind a two-dimensional model with a blunt trailing edge and fitted with splitter plates, J. Fluid Mech. **21**, 241 (1965).

[58] P. W. Bearman, On vortex shedding from a circular cylinder in the critical Reynolds number regime, J. Fluid Mech. **37**, 577 (1969).

[59] P. W. Bearman, Vortex shedding from oscillating bluff bodies, Annu. Rev. Fluid Mech. **16**, 195 (1984).

[60] M. F. Unal and D. Rockwell, On vortex formation from a cylinder. Part 1. The initial instability, J. Fluid Mech. **190**, 491 (1988).

[61] G. Chopra and S. Mittal, Drag coefficient and formation length at the onset of vortex shedding, Phys. Fluids **31**, 013601 (2019).

[62] J. H. Lienhard, Synopsis of lift, drag, and vortex frequency data for rigid circular cylinders, Bulletin (Washington State University. College of Engineering. Research Division), Technical Extension Service, Washington State University, 1966, https://engines.egr.uh.edu/sites/engines/files/talks/vortexcylinders.pdf.

[63] M. Van Dyke, *An Album of Fluid Motion* (Parabolic Press, Stanford, California, 1982).

[64] P. K. Kundu and I. M. Cohen, *Fluid Mechanics*, 4th ed. (Academic Press, 2008).

[65] R. J. Adrian and J. Westerweel, *Particle Image Velocimetry*, Cambridge Aerospace Series, Vol. 30 (Cambridge University Press, New York, 2011).

[66] R. J. Adrian, Particle-imaging techniques for experimental fluid mechanics, Annu. Rev. Fluid Mech. **23**, 261 (1991).

[67] M. Raffel, C. E. Willert, F. Scarano, C. J. Kahler, S. T. Wereley, and J. Kompenhans, *Particle Image Velocimetry*, 3rd ed. (Springer International Publishing, Cham, 2018).

[68] Teensy Timer Tool, Double exposure laser illuminator, Github, 2023, https://github.com/luni64/TeensyTimerTool.

[69] A. Liberzon, D. Lasagna, M. Aubert, P. Bachant, T. Käufer, jakirkham, A. Bauer, B. Vodenicharski, C. Dallas, J. Borg, tomerast, and ranleu, OpenPIV/openpiv-python: OpenPIV-Python v0.25,3 [Computer software], Zenodo, 2024, https://doi.org/10.5281/zenodo.18304582.

[70] J. Westerweel and F. Scarano, Universal outlier detection for PIV data, Exp. Fluids **39**, 1096 (2005).

[71] X. Liu and J. Katz, Instantaneous pressure and material acceleration measurements using a four-exposure PIV system, Exp. Fluids **41**, 227 (2006).

[72] J. J. Charonko, C. V. King, B. L. Smith, and P. P. Vlachos, Assessment of pressure field calculations from particle image velocimetry measurements, Meas. Sci. Technol. **21**, 105401 (2010).

[73] R. de Kat and B. Ganapathisubramani, Pressure from particle image velocimetry for convective flows: A Taylor's hypothesis approach, Meas. Sci. Technol. **24**, 024002 (2013).

[74] B. W. van Oudheusden, PIV-based pressure measurement, Meas. Sci. Technol. **24**, 032001 (2013).

[75] X. Liu, J. R. Moreto, and S. Siddle-Mitchell, Instantaneous pressure reconstruction from measured pressure gradient using rotating parallel ray method, *54th AIAA Aerospace Sciences Meeting* (AIAA, San Diego, California, 2016), p. 1049.

[76] X. Liu and J. R. Moreto, Error propagation from the PIV-based pressure gradient to the integrated pressure by the omnidirectional integration method, Meas. Sci. Technol. **31**, 055301 (2020).

[77] M. Nie, J. P. Whitehead, G. Richards, B. L. Smith, and Z. Pan, Error propagation dynamics of PIV-based pressure field calculation (3): What is the minimum resolvable pressure in a reconstructed field? Exp. Fluids **63**, 168 (2022).

[78] H. Tennekes and J. L. Lumley, *A First Course in Turbulence* (MIT Press, 1972).

[79] S. B. Pope, *Turbulent Flows* (Cambridge University Press, 2000).

[80] K. Chang and G. Constantinescu, Numerical investigation of flow and turbulence structure through and around a circular array of rigid cylinders, J. Fluid Mech. **776**, 161 (2015).

[81] J. Zhou and S. K. Venayagamoorthy, Near-field mean flow dynamics of a cylindrical canopy patch suspended in deep water, J. Fluid Mech. **858**, 634 (2019).

[82] C. Nicolai, S. Taddei, C. Manes, and B. Ganapathisubramani, Wakes of wall-bounded turbulent flows past patches of circular cylinders, J. Fluid Mech. **892**, A37 (2020).

[83] See Supplemental Material at http://link.aps.org/supplemental/10.1103/m9ny-j9bd for additional on information the calculations of bleeding flows, and additional figures as referenced in the main text.

[84] M. S. Bansal and S. Yarusevych, Experimental study of flow through a cluster of three equally spaced cylinders, Exp. Therm. Fluid Sci. **80**, 203 (2017).

[85] K. Lam and W. C. Cheung, Phenomenon of vortex shedding and flow interference of three cylinders in different equilateral arrangements, J. Fluid Mech. **196**, 1 (1988).

[86] B. R. Noack, W. Stankiewicz, M. Morzynski, and P. J. Schmid, Recursive dynamic mode decomposition of a transient cylinder wake, J. Fluid Mech. **809**, 843 (2016).

[87] N. Deng, B. R. Noack, M. Morzynski, and L. R. Pastur, Low-order model for successive bifurcations of the fluidic pinball, J. Fluid Mech. **884**, A37 (2020).

[88] N. Deng, B. R. Noack, M. Morzynski, and L. R. Pastur, Galerkin force model for transient and post-transient dynamics of the fluidic pinball, J. Fluid Mech. **918**, A4 (2021).

[89] M. Hassanalian, A. Mirzaeinia, N. Bawana, and F. Heppner, Energy management of echelon flying northern bald ibises with different wingspans and variable wingtip spacing, J. Bionic Eng. **19**, 44 (2022).

[90] F. Beaumont, S. Murer, F. Bogard, and G. Polidori, Aerodynamic interaction of migratory birds in gliding flight, Fluids **8**, 50 (2023).